2008

Luminous Infrared Galaxies with the Submillimeter Array. I. Survey Overview and the Central Gas to Dust Ratio

CD Wilson

GR Petitpas

D Iono

AJ Baker

AB Peck

See next page for additional authors

Recommended Citation

Wilson, CD; Petitpas, GR; Iono, D; Baker, AJ; Peck, AB; Krips, M; Warren, B; Golding, J; Atkinson, A; Armus, L; Cox, TJ; Ho, P; Juvela, M; Matsushita, S; Mihos, JC; Pihlstrom, Y; and Yun, Min, "Luminous Infrared Galaxies with the Submillimeter Array. I. Survey Overview and the Central Gas to Dust Ratio" (2008). *The Astrophysical Journal Supplement Series*. 1133.
https://doi.org/10.1086/590910

Resubmitted to ApJS

Luminous Infrared Galaxies with the Submillimeter Array: I. Survey Overview and the Central Gas to Dust Ratio

Christine D. Wilson[1,2], Glen R. Petitpas[2], Daisuke Iono[3,2], Andrew J. Baker[4], Alison B. Peck[2,12], Melanie Krips[2], Bradley Warren[1], Jennifer Golding[1], Adam Atkinson[1], Lee Armus[11], T. J. Cox[2], Paul Ho[9,2], Mika Juvela[10], Satoki Matsushita[9], J. Christopher Mihos[8], Ylva Pihlstrom[7], Min S. Yun[6]

ABSTRACT

We present new data obtained with the Submillimeter Array for a sample of fourteen nearby luminous and ultraluminous infrared galaxies. The galaxies were selected to have distances $D_L < 200$ Mpc and far-infrared luminosities $\log L_{\rm FIR} > 11.4$. The galaxies were observed with spatial resolutions of order

[1]Department of Physics & Astronomy, McMaster University, Hamilton, Ontario L8S 4M1 Canada; wilson@physics.mcmaster.ca, bwarren@physics.mcmaster.ca, goldingj@physics.mcmaster.ca, atkinsa@muss.cis.mcmaster.ca

[2]Harvard-Smithsonian Center for Astrophysics, Cambridge, MA 02138; gpetitpa@cfa.harvard.edu, mkrips@cfa.harvard.edu, tcox@cfa.harvard.edu

[3]National Astronomical Observatory of Japan, 2-21-1 Osawa, Mitaka, Tokyo 181-0015, Japan; d.iono@nao.ac.jp

[4]Department of Physics and Astronomy, Rutgers, the State University of New Jersey, 136 Frelinghuysen Road, Piscataway, NJ 08854-8019 U.S.A.; ajbaker@physics.rutgers.edu

[6]Department of Astronomy, University of Massachusetts, Amherst, MA 01003;myun@astro.umass.edu

[7]Department of Physics and Astronomy, University of New Mexico, Albuquerque, NM 87131; ylva@unm.edu

[8]Department of Astronomy, Case Western Reserve University, 10900 Euclid Avenue, Cleveland, OH 44106; mihos@case.edu

[9]Academia Sinica Institute of Astronomy and Astrophysics, Taipei 106, Taiwan; pho@asiaa.sinica.edu.tw, satoki@asiaa.sinica.edu.tw

[10]University of Helsinki Observatory, Finland; mika.juvela@helsinki.fi

[11]Spitzer Science Center, California Institute of Technology, Pasadena, CA 91125; lee@ipac.caltech.edu

[12]Joint ALMA Office, Avda El Golf 40, piso 18, Santiago, Chile 7550108; apeck@alma.cl

1 kpc in the CO J=3-2, CO J=2-1, ^{13}CO J=2-1, and HCO$^+$ J=4-3 lines as well as the continuum at 880 μm and 1.3 mm. We have combined our CO and continuum data to measure an average gas-to-dust mass ratio of 120 ± 28 (rms deviation 109) in the central regions of these galaxies, very similar to the value of 150 determined for the Milky Way. This similarity is interesting given the more intense heating from the starburst and possibly accretion activity in the luminous infrared galaxies compared to the Milky Way. We find that the peak H_2 surface density correlates with the far-infrared luminosity, which suggests that galaxies with higher gas surface densities inside the central kiloparsec have a higher star formation rate. The lack of a significant correlation between total H_2 mass and far-infrared luminosity in our sample suggests that the increased star formation rate is due to the increased availability of molecular gas as fuel for star formation in the central regions. In contrast to previous analyses by other authors, we do not find a significant correlation between central gas surface density and the star formation efficiency, as trace by the ratio of far-infrared luminosity to nuclear gas mass. Our data show that it is the star formation rate, not the star formation efficiency, that increases with increasing central gas surface density in these galaxies.

Subject headings: galaxies: infrared — galaxies: individual (Arp 55, Arp 193, Arp 299, IRAS 10565+2448, IRAS 17208-0014, Mrk 231, Mrk 273, NGC 1614, NGC 2623, NGC 5331, NGC 5257, NGC 5258, NGC 6240, UGC 5101, VV 114)

1. Introduction

Ultra-luminous infrared galaxies (ULIRGs) contain the regions of most intense star formation in the local universe. Although their high rates of star formation and accretion appear to be triggered by the merger of two gas-rich galaxies (Sanders et al. 1988a; Veilleux et al. 2002), the detailed physical connection between galaxy mergers and star formation and, in particular, the time evolution of this process, is not well understood. Relating numerical hydrodynamical models (Mihos & Hernquist 1996; Cox et al. 2004) to observations is complicated by the difficulty in identifying the precise stage of the merger (Murphy et al. 2001). In addition, while high resolution imaging has found that most ULIRGs have nuclear separations from <0.3 kpc to 48 kpc (Murphy et al. 1996), other strongly interacting galaxies with these nuclear separations which are *not* ULIRGs have also been found (Braine et al. 2004). These observations suggest that the onset of the intense star formation and accretion which produces a ULIRG is not a simple function of the age of the merger and leaves open

the question of whether all luminous infrared galaxies (LIRGs[1]; $11 \leq \log(L_{\rm FIR}/L_{\odot}) < 12$) will pass through a ULIRG phase ($\log(L_{\rm FIR}/L_{\odot}) \geq 12$) at some point in their evolution.

Local ULIRGs are also important as the closest analogs to the high-redshift submillimeter galaxies (SMGs; Blain et al. 2002): both populations have high infrared luminosities, large amounts of molecular gas (Frayer et al. 1998, 1999; Neri et al. 2003; Greve et al. 2005; Tacconi et al. 2006), and morphological evidence of recent or ongoing mergers (Veilleux et al. 2002; Conselice et al. 2003). Since galaxy merger rates are substantially higher in the early universe (Le Fèvre et al. 2000; Gottlöber et al. 2001), understanding the physical and dynamical properties of nearby ULIRGs is also important for understanding the processes in the early universe which give rise to the very luminous submillimeter galaxy population.

Because molecular gas is the fuel for current and future star formation, the physical properties and distribution of the warm, dense molecular gas are crucial for understanding the processes and timescales controlling star formation in galaxy mergers. Previous high-resolution studies of molecular gas in luminous infrared galaxies have used primarily the ground-state rotational transition of CO, which is sensitive to gas as cold as 10 K (Scoville et al. 1991; Downes & Solomon 1998; Bryant & Scoville 1999), with a few galaxies observed in the CO J=2-1 line (Bryant & Scoville 1996; Downes & Solomon 1998; Sakamoto et al. 1999; Tacconi et al. 1999). However, since the CO J=3-2 line traces the warmer and denser gas, it is more likely to be directly associated with the starburst activity and/or fueling of the active galactic nuclei (AGN) in these galaxies. Indeed, observations of the CO J=3-2 emission in two luminous infrared galaxies, VV 114 (Iono et al. 2004) and NGC 6090 (Wang et al. 2004), reveal that the large-scale distribution and kinematics of the CO J=3-2 line can be significantly different from those of the CO J=1-0 line.

In this paper, we present new data obtained with the Submillimeter Array (SMA) for a sample of fourteen luminous and ultraluminous infrared galaxies in the CO J=3-2, CO J=2-1, ^{13}CO J=2-1, and HCO$^+$ J=4-3 lines. In addition, we present new high-resolution observations of continuum emission at 880 μm and 1.3 mm, which allow us to study the dust properties in the central kiloparsec of the galaxies. This SMA legacy survey aims to address five broad scientific questions:

1. *What are the distributions, kinematics, and physical conditions of dense molecular gas in U/LIRGs?* The high resolution CO J=3-2 data cubes trace the distribution of the warm and dense gas that feeds the starburst (and any accretion) activity in

[1] $L_{\rm FIR} = 4\pi D_L^2 F_{\rm FIR}\ L_{\odot}$, where $F_{\rm FIR} = 1.26 \times 10^{-14}(2.58 f_{60} + f_{100})$ erg cm^{-2} s^{-1} and f_{60} and f_{100} are the IRAS fluxes in Jy at 60 and 100 μm (Sanders & Mirabel 1996).

these luminous galaxies. The new SMA CO J=3-2, J=2-1, and ^{13}CO J=2-1 data can be combined with published CO J=1-0 and J=2-1 data for a detailed investigation of the physical properties of the molecular gas using Large Velocity Gradient (LVG, Scoville & Solomon 1974; Goldreich & Kwan 1974) and Monte Carlo (Juvela 1997) models as our primary diagnostic tools. The CO J=3-2 kinematics allow us to study the detailed gas dynamics in the inner few hundred parsecs, yielding measurements of the total enclosed mass and of the local linewidth that is a parameter in models of disk turbulence. The combination of morphology and kinematics offers clues to the geometry of each merger via comparison of the separation and orientation of the galaxy nuclei with the results from numerical simulations (see, e.g., Mundell et al. 2001, for an analysis of Arp 220) .

2. *What is the distribution of the dust in U/LIRGs?* The 880 μm continuum images trace the spatial distribution of the cold and warm (10–70 K) dust, which reflects both the local rate of star formation activity and the available mass of gas. The submillimeter dust emission is often significantly more compact than that of CO (e.g., Sakamoto et al. 1999; Meier & Turner 2001; Sakamoto et al. 2006) arising exclusively from deep in the gravitational potential wells of the galactic nuclei. High-resolution continuum images from the SMA can be combined with spectra from the *Spitzer Space Telescope* (e.g., Armus et al. 2007) to estimate the dust temperature via the mid-infrared to submillimeter spectral energy distribution (SED), the dust mass (including both small and large grains, e.g., Marshall et al. 2007) and, indirectly, the gas mass based on 3D radiative transfer modeling (Juvela & Padoan 2003). In addition, these spatially resolved SEDs of local U/LIRGS will improve our interpretation of the templates used for determining photometric redshifts of high-redshift submillimeter galaxies (Yun & Carilli 2002; Aretxaga et al. 2003, 2005).

3. *Do the gas properties change as the interaction progresses?* Our sample of fourteen U/LIRGs covers a range from mid to late merger stages and should be sufficiently large that we can establish a merger sequence through comparison of global morphologies with numerical models (Mihos & Hernquist 1996; Cox et al. 2004). This data set allows us to determine how the distribution and kinematics of the gas change as a function of physical conditions such as density and temperature, or vice versa, and to correlate those changes with the stage of the merger. This type of detailed gas physics on small scales still poses challenges for numerical simulations. Thus, on large scales, where the dynamics of the system are well described by the models, the numerical simulations can help with the interpretation of the data, while on smaller scales, the data can drive the development of more accurate descriptions for the gas physics in the simulations.

4. *How do the properties of the dense gas in local U/LIRGs compare to those of the gas in high-redshift submillimeter galaxies?* Armed with a robust local sample of fourteen U/LIRGs, we can make a rigorous comparison of the properties of the gas with those in higher redshift galaxies (Greve et al. 2005; Tacconi et al. 2006). Changes in gas characteristics over the age of the universe will reveal important information about the process of star formation and ultimately the formation and evolution of galaxies at early times.

5. *What is the origin of nuclear OH megamasers?* Bright 1667 MHz OH megamaser emission is observed in the nuclei of some luminous infrared galaxies, including five galaxies in our sample (IRAS 17208-0014, Mrk 231, Mrk 273, UGC 5101 and Arp 299). These extremely bright masers are promising tracers of dust-obscured star formation and mergers at high redshifts, and could ultimately be used to estimate the merger rate as a function of redshift (Darling & Giovanelli 2002). However, in order to use OH megamasers as high-redshift probes, we need to understand whether there is a specific type or stage of merger that leads to OH maser emission. Whether maser emission occurs is likely governed by the physical, chemical, and kinematic conditions in the molecular gas in the nuclear regions of the mergers. For example, using global CO and HCN luminosities, Darling (2007) concludes that OH megamasers are associated with high mean molecular gas densities and high dense gas fractions. Our sample, which contains galaxies with and without megamasers, is well suited for identifying any unique nuclear conditions that produce OH megamasers in luminous infrared galaxies.

In this paper, we describe the sample selection, observations, and reduction of the survey data (§ 2). We also examine the gas to dust mass ratio in the central kiloparsec (§ 3) and correlations between the central gas mass, gas surface density, infrared luminosity, dust temperature, and CO J=3-2/2-1 line ratio (§ 4). A companion paper presents a detailed analysis of the galaxy VV 114 (Petitpas et al. 2008); a detailed analysis of NGC 6240 is given in Iono et al. (2007). Future papers will compare the results from this survey with similar observations of high-redshift submillimeter galaxies (Iono et al. 2008); examine the physical properties of the molecular gas by combining molecular line observations with radiative transfer models; use the molecular gas data to place constraints on the origin of the OH megamaser activity seen in some of the galaxies in our sample; compare the properties of the cold gas and dust as seen with the SMA with the properties of the warm dust derived from *Spitzer* data; and compare the molecular gas and dust properties with the predictions of numerical simulations to place the galaxies into a merger sequence.

2. Observations and Data Reduction

2.1. Sample selection

For this survey, we selected a sample of luminous and ultraluminous infrared galaxies with redshifts $z < 0.045$ (distances $D_L < 200$ Mpc, adopting $H_o = 70$ km s^{-1} Mpc^{-1}, $\Omega_M = 0.3$, $\Omega_\Lambda = 0.7$) and far-infrared luminosities $\log L_{\rm FIR} > 11.4$. The distance limit was chosen to allow spatial resolutions of order 1 kpc or better in all the target galaxies. The luminosity cutoff was chosen to allow us to span a wide range of merger properties and luminosities while still concentrating on the most infrared-luminous nearby galaxies. Out of a total of 39 galaxies above declination -20^o (Sanders et al. 2003) which meet these two criteria, we selected for this survey 14 galaxies with previous interferometric observations in the CO J=1-0 transition. The galaxies observed in this survey are listed in Table 1 and shown in Figure 1. The sample includes five systems in which the two progenitor galaxies are still distinct (Arp 299, Arp 55, VV 114, NGC 5331, and NGC 5257/8); the remaining nine galaxies show a single central concentration.

Compared to the full sample of 39 galaxies, the sample observed with the SMA has a much higher fraction of galaxies with a large far-infrared flux (86% with $F_{\rm FIR} > 45$ Jy compared to 44% for the full sample). The SMA sample contains a higher proportion of nearby galaxies (29% with $z < 0.021$ compared to 15% for the full sample), although the mean distance of the SMA sample is only 4% smaller than the mean distance of the full sample. The SMA sample also has a higher proportion of more luminous galaxies (29% with $\log L_{\rm FIR} > 11.9$ compared to 13% for the full sample), and has a mean far-infrared luminosity that is 35% larger (0.13 in $\log L_{\rm FIR}$) than the full sample. Thus, the sample of galaxies discussed in this paper is slightly biased towards more luminous galaxies than the full luminosity and distance limited sample.

2.2. Data from the Submillimeter Array

Observations with the Submillimeter Array (SMA: Ho et al. 2004) were obtained between 2005 May 16 and 2007 May 2. The correlator was configured to have a spectral resolution of 0.8125 MHz (typically ~ 0.7 km s^{-1} for CO J=3-2 and ~ 1.1 km s^{-1} for CO J=2-1) and a bandwidth of 2 GHz, which was covered by 24 "chunks" overlapping slightly in frequency in each of the upper and lower sidebands. Each galaxy was observed with the CO J=3-2 transition in the lower sideband of the receiver and continuum in the upper sideband, 10 GHz away. The HCO^+ J=4-3 line lies in the high-frequency end of the upper sideband window and was detected in seven of the galaxies in our sample. In addition, nine galaxies

were observed in the CO and ^{13}CO J=2-1 lines and in 1.3 mm continuum in a single tuning. It was not possible to also include the C^{18}O J=2-1 line in our passband due to the broad lines of these galaxies.

Each galaxy was observed in a single configuration of the SMA, either the extended array (unprojected baselines of 50 to 182 m) or the compact array (unprojected baselines of 16 to 69 m). The largest angular scale to which these data are sensitive, as calculated from the minimum *uv* distance that the data sample well, ranges from 12-16″ (19-25″) for the compact array CO J=3-2 (J=2-1) data to 7-10″ (10-15″) for the extended array CO J=3-2 (J=2-1) data. The configuration used in each case was chosen to yield a spatial resolution of 0.7-1 kpc in the CO J=3-2 line; the typical angular resolution at this wavelength is 2.5″ for the compact configuration and 0.9″ for the extended configuration. The exceptions were NGC 2623 in CO J=2-1, and NGC 6240 and IRAS 17208-0014 in CO J=3-2, which were observed in both the extended and compact arrays, and NGC 5257/8, which was observed in both the compact and sub-compact arrays. For a given galaxy, the same configuration was used for both the CO J=2-1 and the CO J=3-2 observations. The field of view of the SMA is $\sim 60''$ for the CO J=2-1 data and $\sim 40''$ for the CO J=3-2 data. Three of the galaxies have sufficiently extended CO emission that a small mosaic of two (Arp 299, NGC 5331) or three (NGC 5257/58) pointings was used.

The data for each line-configuration combination in each galaxy were obtained in a single night's observing except for NGC 2623 (CO J=2-1 extended array data), NGC 5257/8 (CO J=3-2 data), and VV 114 (CO J=2-1 data). Between 6 and 8 antennas were used in the observations and the total on-source integration time ranged from 3.0 to 13.0 hr. The typical double sideband system temperatures at transit ranged from 240 to 800 K for the CO J=3-2 data, except for IRAS 17208-0014, for which the values ranged from 650 to 1900 K, and from 140 to 550 K for the CO J=2-1 data. The observing dates, on-source integration times, and sensitivities obtained with robust weighting are given in Table 2.

The initial data calibration was done using the MIR software package. Observations of Uranus, Neptune, Ganymede, or Callisto were used to determine the current flux of the gain calibrator, which was a nearby quasar with a flux of at least 0.6 Jy. The amplitude and phase gain variations with time were calibrated using this gain calibrator. Antenna-based gain solutions were used throughout except for the extended array observations of NGC 2623 which required baseline-based gain solutions. Bandpass calibration was determined using a strong quasar such as 3C273, 3C279, or 3C111. We estimate the absolute flux calibration accuracy of these data to be 20%. However, some of the galaxies are at redshifts such that ozone lines affect the atmospheric transmission in the CO J=3-2 line (Arp 55, UGC 5101) or 880 μm continuum (Arp 299, Mrk 273, and, to a lesser extent, Arp 55, Mrk 231, NGC 5331,

and UGC 5101, for which only 200 MHz of the continuum bandwidth might be affected); thus, the absolute calibration for these galaxies is more uncertain. After calibration in MIR, the data were exported to MIRIAD format (Sault et al. 1995) for further editing and imaging.

The data were first flagged to remove the six beginning and ending channels of each of the 24 chunks of the correlator. The data were also flagged to remove high amplitude data points, with typically $< 1\%$ of the data removed in this step. For a few data sets, additional flagging was used to remove data at the beginning or end of the track when deteriorating weather conditions or high system temperatures at lower elevations had caused a larger amplitude scatter. Data cubes were made using velocity resolutions of 10, 20, and 40 km s^{-1} for the CO J=3-2 and J=2-1 lines, 20, 40, and 100 km s^{-1} for the ^{13}CO J=2-1 line, and 40 and 100 km s^{-1} for the HCO^+ J=4-3 line. For the ^{13}CO J=2-1 and HCO^+ data sets where significant continuum emission was detected (see below), the continuum emission was subtracted in the *uv* plane using line-free channels before imaging. All data cubes were inverted with weighting by the system temperature and moderate robustness, which gives the optimal tradeoff between sensitivity and resolution.

Each data cube was cleaned down to two times the rms noise, except for NGC 6240, which was cleaned down to the rms noise. For most sources, the beam was sufficiently clean and the emission sufficiently compact that cleaning the inner quarter of the image produced good results. However, four sources located near the equator (IRAS 17208-0014, NGC 5331, NGC 5257, and NGC 6240) had large sidelobes and/or extended emission and were cleaned using regions chosen by inspecting the dirty maps to isolate the emission from the galaxy; the same fixed regions were used for all velocity channels. The final data cubes were corrected for the attenuation of the SMA primary beam or the analgous response for the combined mosaic before we measured the integrated source fluxes.

Continuum maps at 1.3 mm and 880 μm were made by imaging the individual line-free regions of the spectra; there were four such regions at 1.3 mm (one on either side of each of the CO and ^{13}CO J=2-1 lines) and three regions at 880 μm (one on either side of the CO J=3-2 line and a single broad region in the upper sideband that excluded the region of the spectrum containing possible emission from the HCO^+ J=4-3 line). These continuum images were then averaged together, weighting by the inverse of the product of the bandwidth of each image and the square of its noise, to obtain a single continuum image with the best sensitivity. The continuum images were not cleaned, as the signal-to-noise ratio was low and the source(s) were generally compact and well separated from any sidelobes of the main beam. The one exception is Mrk 231, where the central source was sufficiently strong that cleaning was useful.

Table 3 gives the continuum and integrated ^{12}CO, ^{13}CO, and HCO$^+$ fluxes measured for the galaxies in our sample. The fluxes measured for the CO J=3-2 line and 880 μm continuum emission for NGC6240 differ somewhat from the values given in Iono et al. (2007) due to the different weighting used. Previously published data for the CO J=2-1 and J=1-0 lines are also given where available. Figures 2-24 show the moment 0, 1, and 2 images for the CO J=3-2 and CO J=2-1 data, the 880 μm and 1.3 mm dirty maps where signal was detected from the galaxy at the 3σ level or better, and the ^{13}CO J=2-1 and HCO$^+$ J=4-3 integrated intensity maps, where these lines were detected. Unless otherwise noted in the figure captions, the moment 0 maps have been made from the 40 km s^{-1} resolution data cube using only signal greater than $\pm 2\sigma$, while the moment 1 and 2 maps have been made from the 20 km s^{-1} resolution data cube using only positive signal greater than 4σ. These images have not been corrected for the primary beam or mosaic response. Figures 25-29 show the CO J=3-2 spectra, Figures 30-33 show the CO J=2-1 spectra, Figures 34-35 show the ^{13}CO J=2-1 spectra and Figure 36 shows the HCO$^+$ J=4-3 spectra. In all cases except HCO$^+$, both the spectrum at the position of the emission peak and the spectrum integrated over the entire region with emission are shown.

2.2.1. Morphology and kinematics of the CO emission

Figures 2-24 reveal a diversity of morphologies and kinematics for the molecular gas in our sample of galaxies. Nine of the galaxies show a predominantly compact morphology while the remaining five galaxies range from well-separated pairs of galaxies to highly complex morphologies. The galaxies with extended CO emission are all found in the lower luminosity half of our sample, although some low luminosity galaxies also show a compact morphology. The source sizes derived from two-dimensional Gaussian fits to the CO J=3-2 images and the line widths (full width at half maximum) derived from the CO J=3-2 spectra are tabulated in Iono et al. (2008). The distributions of the CO J=3-2 and J=2-1 emissions are qualitatively similar; we will discuss the line ratio distributions in more detail in a future paper.

The kinematics of the molecular gas are also quite varied. Integrating over the full emission region in each galaxy (Figures 25-33), the line widths at half maximum range from 200 km s^{-1} in Mrk 231 to 650 km s^{-1} in UGC 5101. Some of the line profiles are quite smooth and gaussian (e.g. Mrk 231), while others have more of a double-peaked structure (e.g. UGC 5101). The maps of the velocity fields (Figures 2-24) show many examples of smooth and regular rotation among the more compact galaxies, although some of the compact galaxies, such as Mrk 273 and NGC 6240, are significantly distorted. Two of the galaxies with extended CO emission, Arp 299 and VV 114 show very complex and distorted

velocity fields. The maps of the velocity dispersions show that the peak velocity dispersion is commonly 80-100 km s^{-1}. However, the peak velocity dispersions for IRAS 17208-0014, Mrk 273, UGC 5101, NGC6240, and NGC 5331S are twice as large as the typical galaxy in our sample. The lower velocity dispersions seen for NGC 5257/8 are likely due to the lower signal-to-noise of those maps; similarly, a lower velocity dispersion is seen for NGC 5331S in the CO J=3-2 line than in the CO J=2-1 line.

Our velocity dispersions are typically about 70% of the values measured from CO band-head emission in the near-infrared (Hinz & Rieke 2006; Dasyra et al. 2006). In some cases, the lower values found in this paper may be related to the somewhat lower angular resolution of the millimeter-wave CO observations, as discussed by Hinz & Rieke (2006). The near-infrared data may also overestimate the velocity dispersion if the CO band-head emission is strongly peaked on the nucleus (Hinz & Rieke 2006). We derive a significantly larger velocity disperion for IRAS 17208-0014; this may be due to the lower signal-to-noise ratio of the near-infrared spectrum for this galaxy.

2.2.2. The relative strength of the HCO$^+$ J=4-3 emission

We detect the HCO^+ J=4-3 line in seven of the fourteen galaxies in our sample. Since the weak HCO^+ emission is extremely compact, we compare the line strength to the peak line strength of the CO J=3-2 line. The CO/HCO^+ line ratios are 8 and 16 for Mrk 231 and NGC 2623, respectively, and range from $\leq$7 to $\leq$32 for the other five galaxies. Treating all the HCO^+ lines as detections rather than upper limits, and treating the detections of the eastern and central components of VV114 separately, the average line ratio is 19 with an rms deviation of 9. However, the true average line ratio for these galaxies is likely somewhat smaller, since many of the HCO^+ detections are lower limits because the line emission extends to the edge of the spectral window.

This line ratio is comparable to the average CO/HCO^+ line ratio using the J=1-0 and J=3-2 lines, respectively, determined for 6 of the galaxies in our sample by Graciá-Carpio et al. (2006), who also find a roughly constant CO/HCO^+ line ratio as a function of L_{FIR}. High-resolution HCO^+ J=1-0 data have been published for four of the galaxies in our sample by Imanishi et al. (2006, 2007). Comparing their data with our new measurements yields HCO^+ J=4-3/J=1-0 line ratios of about 4 in both Mrk231 and Arp 299, while this same line ratio appears to vary dramatically from place to place within VV 114. The HCN/HCO^+ J=1-0 line ratio also varies spatially in VV 114 (Imanishi et al. 2007) and in Arp 299 (Imanishi et al. 2006), which suggests that there are interesting physical and/or chemical variations in the gas properties in these early-stage mergers. Large variations in the HCN J=4-3/J=1-0 ratio

in a sample of four galaxies are evidence for significant differences in the excitation in the gas phase (Papadopoulos 2007).

The seven galaxies detected in HCO^+ are the galaxies with strong centrally peaked lines, for which the ratio of the CO peak flux to the full-width half-maximum of the line is greater than 1 (Table 7 and Figure 25-29). Thus, it appears that we have detected HCO^+ in all the galaxies in our sample where we have sufficient sensitivity to detect the peak of the line in a single channel. The fact that the remaining galaxies are not detected may be attributed to insufficient sensitivity; while it is possible that some of these galaxies may be relatively weak in HCO^+ compared to CO, we have no direct evidence of any such line ratio variations.

2.2.3. The relative strength of the ^{13}CO J=2-1 emission

Of the nine galaxies observed at 230 GHz with the SMA, we have detected ^{13}CO J=2-1 emission in only four galaxies: Arp 299, VV 114, NGC 5331S, and NGC 1614. All of these galaxies except NGC 5331S were also detected in HCO^+; the only galaxy that was observed at 230 GHz and detected in HCO^+ but *not* in ^{13}CO is NGC 2623. This is likely because NGC 2623 is less luminous in CO J=2-1 (compare NGC 2623 with NGC 1614 in Table 3). Given the average strength of the ^{13}CO line compared to the CO line in our four detections, we would not expect to detect any of the remaining galaxies in our sample at the 3 sigma level or better.

2.3. Published and Archival Single-Dish Data

In this section, we summarize published single-dish data for the CO J=3-2 line and 880 μm continuum from the James Clerk Maxwell Telescope (JCMT). To these published results we add unpublished continuum and spectral line data taken from the JCMT archive. The sample of single-dish data for the CO J=2-1 line and 1.3 mm continuum is less complete; the available data will be discussed in a future paper.

2.3.1. Single-Dish CO J=3-2 Data

A search of the JCMT archive reveals that many of the galaxies in our sample have been observed in the CO J=3-2 line with the JCMT with a 15″ beam. In addition, we used the JCMT to make small (7x7) Nyquist-sampled maps (program M05AC05) or 2′ Nyquist-sampled maps with the new array receiver HARP-B (program M07AC11) of many of our

galaxies in the CO J=3-2 line. Our ultimate goal is to combine these single-dish data with our SMA data to obtain complete maps without any missing spatial frequencies. An example and discussion of this technique as applied to VV 114 is given in Petitpas et al. (2008). These maps also can be used to estimate the total CO J=3-2 emission from some of our galaxies. By combining our new data with archival data, we can obtain single-dish CO J=3-2 spectra for all the galaxies in our sample except NGC 5331.

The quality of the data varies quite significantly from one galaxy to another. For three galaxies (VV 114, NGC 2623, NGC 1614), we have maps covering 35″ on a side that clearly include all the emission from the galaxy. For Arp 299 and NGC 5258, we have maps covering 2′ on a side but with bad baselines in some of the outer pixels; in addition, these data needed to be scaled up by a factor of 1.25 to make observations of spectral line standards consistent with previous results. We also adopt a higher calibration uncertainty (30%) for these data sets. Mrk 273, Mrk 231, IRAS 10565+2448, UGC 5101, IRAS 17208-0014, NGC 6240, and Arp 193 were all observed in a single co-ordinated program in 1999 (program M99AN19, PI. Papadopoulos) with many observations of calibrators to check for calibration consistency. Arp 55 has only a single spectrum centered roughly on the south-western source that is visible in our interferometric maps (Figure 11). This flux measurement must be considered a lower limit since this pointing would detect very little emission from the stronger northern source. For NGC 5257, there is a single spectrum published in Yao et al. (2003). We reduced these data again (program M01AC03, PI Seaquist), including the calibration data, and there appear to be some problems with the calibration during these observations. The main beam efficiency is 20% lower than the standard value and the observations of the spectral line standards are also lower by about a similar amount. Although we have corrected for these effects in calculating the CO flux, the calibration must be considered more uncertain for this galaxy.

In converting the single-dish fluxes from their intrinsic units of K(T_A^*) km s^{-1} to Jy km s^{-1}, we assume an aperture efficiency of 0.5, which gives a scaling factor of 31.3 Jy K^{-1}. All of the galaxies in our sample that have not been mapped are sufficiently compact that we assume a point-source distribution in converting from K to Jy. The exception is Arp 55, for which we assume the emission fills the main beam of the telescope and thus divide by the main beam efficiency $\eta_{MB} = 0.63$ before multiplying by 31.3 Jy K^{-1}. For the four galaxies with small maps, each spectrum was converted to Jy km s^{-1} using the point source scaling factor, and then the spectra were summed and normalized by the number of pixels per 15″ beam in the map to obtain the final integrated flux. The resulting single-dish CO J=3-2 fluxes are given in Table 4.

2.3.2. Single-Dish 880 μm Data

Published 850 or 800 μm fluxes from the JCMT are available for all the galaxies in our sample except NGC 5331 and Arp 299. Data presented by Rigopoulou et al. (1996) for Mrk 231, Mrk 273, and UGC 5101 were obtained with the single-pixel bolometer UKT14 at 800 μm, while data from Klaas et al. (2001) for IRAS 17208-0014 and NGC 6240 and Dunne et al. (2000) for the remaining galaxies were obtained with the bolometer array SCUBA at 850 μm. In addition, SCUBA data for VV 114, NGC 5331, and Arp 299 are available in the JCMT archive. These data were processed into images using an automatic pipeline (Di Francesco et al. 2008) and the fluxes were measured by us from those images.

We then rescaled the fluxes by dividing by a factor of 1.13 ± 0.02 (850 μm) or 1.40 ± 0.06 (800 μm) to obtain an estimate of the continuum flux at 880 μm. These scaling factors assume a dust emissivity $\beta = 1.5 \pm 0.5$. The resulting single-dish 880 μm continuum fluxes are given in Table 5. The published uncertainties vary somewhat in their meaning from author to author. Klaas et al. (2001) simply adopt an uncertainty of 30%. The errors given by Rigopoulou et al. (1996) and for VV 114, NGC 5331, and Arp 299 are purely statistical measurement errors with no calibration uncertainty added in. The errors given by Dunne et al. (2000) include a calibration uncertainty of 10% (15% for NGC 5257 and NGC 5258). In comparing the single-dish and SMA fluxes, we have adopted a 20% calibration uncertainty for each telescope and adjusted the published uncertainties for the single-dish data accordingly.

2.4. Comparison of interferometric and single-dish fluxes

A comparison of the CO J=3-2 fluxes recovered by the SMA with the fluxes seen by the JCMT shows that the interferometric data miss a significant fraction of the CO J=3-2 emission for eight of the galaxies in our sample. In these galaxies, we are typically missing 50% of the total single-dish flux. However, only for three galaxies in our sample, Arp 299, VV 114, and NGC 1614, does this missing flux manifest itself as significant negative bowls in the moment maps (Figures 9, 15, and 23). These are the three galaxies with the largest absolute amount of missing flux and so it makes sense that they are the ones in which the missing flux leaves a detectable negative signal in the maps.

We can also calculate the percentage of continuum flux missed by the interferometric observations by comparing the continuum flux detected with the SMA to the single-dish continuum flux detected with the JCMT. In doing this calculation, we also correct for the contribution of the CO J=3-2 line within the SCUBA filter using the formula given by

Seaquist et al. (2004). The results given in Table 5 show that, while the interferometric observations detect all of the single-dish continuum flux in four galaxies (and possibly in a fifth, NGC 5258, if the off-nuclear continuum source is not time variable), for the remaining nine galaxies typically 50-80% of the continuum flux is missed by the interferometer.

This result is somewhat surprising, as the few sources studied previously at millimeter wavelengths at high resolution show quite compact continuum emission. For example, Sakamoto et al. (1999) detect all the 1.3 mm continuum emission in Arp 220 and find it is contained in two compact components associated with the merging nuclei. For Mrk 231, Downes & Solomon (1998) also detect all of the 1.3 mm continuum emission seen in single-dish data (Carico et al. 1992), although in this case the emission is thought to be primarily non-thermal emission from the central AGN, with thermal emission from dust contributing only 20% of the total flux. Mrk 273 and Arp 193 have also been detected at 1.3 mm by Downes & Solomon (1998), but there are no single-dish data for these galaxies that can be used to determine the total flux.

The large amount of missing continuum flux in many of our sample galaxies suggests that a significant fraction of the 880 μm emission occurs on moderately large spatial scales even in systems with very luminous compact cores. (The 15″ beam of the JCMT subtends 3-14 kpc at the distances of the galaxies in our sample.) A plot of the percentage of flux missing at 880 μm versus the percentage missing in the CO J=3-2 line (not shown) shows reasonable agreement for all galaxies, although on average there is a slightly higher percentage of the total flux missing in the continuum images. The good agreement between the percentage of missing flux seen in the CO J=3-2 line and the 880 μm continuum suggests that the missing continuum flux comes from dust emission associated with molecular gas in the more extended disks of the galaxies. Such gas could be associated with a disk-wide starburst (as opposed to a nuclear starburst) or more quiescent star formation as is seen in less luminous spiral galaxies. The difference between our results and previous results for Arp 220 and Mrk 231 is likely due to the fading contribution from dust emission at 1.3 mm combined with the importance of non-thermal and possibly free-free emission in these two galaxies.

3. The Gas-to-Dust Mass Ratio in the Nuclear Regions

We can use our new CO J=3-2 and 880 μm data to estimate the gas and dust masses, and in particular the gas-to-dust mass ratio, in the central regions of these luminous infrared galaxies. The gas-to-dust ratio is interesting because it allows us to probe the physical properties of the interstellar medium on kiloparsec scales in regions of galaxies with intense heating from starburst activity and (perhaps) vigorous accretion. Alternatively, it can be

used to provide an independent check of the gas masses determined from the CO emission lines. The gas mass in the central region is a critical quantity for understanding the evolution of these galaxies, as it determines the fuel for the current activity, be it a central starburst or accretion onto an active nucleus.

3.1. Gas and Dust Mass Calculations

We have calculated the dust mass from the 880 μm flux assuming a dust emissivity at 880 μm, $\kappa = 0.9$ cm^2 g^{-1}, appropriate for molecular cloud envelopes (Henning et al. 1995; Johnstone et al. 2000). With this assumption, the dust mass is given by

$$M_{dust} = 74220 S_{880} D_L^2 (\exp(17/T_D) - 1)/\kappa \ (\mathrm{M}_\odot) \quad (1)$$

where S_{880} is the 880 μm flux in Jy and D_L is the luminosity distance in Mpc. We calculated the dust temperature, T_D, from optically thin modified black-body fits to published global photometric data between 60 and 800 μm, following the procedure of Klaas et al. (2001). Our derived temperatures for Mrk 231, Mrk 273, UGC 5101, and NGC6240 are between 5 K and 10 K warmer than the temperature of the cold component derived by Armus et al. (2007). However, our temperatures are generally in good agreement (except for Mrk231, for which we are 8 K colder) with the values derived by Yang & Phillips (2007) in fits including new data at 350 μm.

To calculate the molecular hydrogen gas mass from the CO J=3-2 emission line, we need to know the CO-to-H_2 conversion factor, X_{CO}. While this conversion factor is now reasonably well determined for normal galaxies (Strong et al. 1988; Wilson & Scoville 1990; Strong & Mattox 1996; Dame et al. 2001; Rosolowsky et al. 2003), it has been clear for many years that the standard conversion factor does not apply to starbursting systems like the galaxies studied here (Bryant & Scoville 1996; Downes & Solomon 1998). In addition, the conversion factor has been determined for the CO J=1-0 line only. To apply the appropriate conversion factor to our CO J=3-2 data also requires us to know or assume an appropriate CO J=3-2/J=1-0 line ratio.

To calculate the H_2 gas mass, we adopt the revised conversion factor advocated by Downes & Solomon (1998), $M_{\mathrm{H_2}} = 0.8 L'_{\mathrm{CO}}(1-0)$, where $M_{\mathrm{H_2}}$ is the H_2 gas mass in $M_\odot$ and $L'_{\mathrm{CO}}(1-0)$ is the luminosity of the CO J=1-0 line in K km s^{-1} pc^2. [This equation corresponds to a CO-to-H_2 conversion factor of 0.5×10^{20} H_2 cm^{-2} (K km s^{-1})$^{-1}$.] To convert our measurements in Jy km s^{-1} to units of K km s^{-1} pc^2, we use the equation

$$\frac{L'}{\mathrm{K\ km\ s^{-1}\ pc^2}} = 3.2546 \times 10^7 (\frac{S_{\mathrm{CO}}}{\mathrm{Jy\ km\ s^{-1}}})(\frac{D_L}{\mathrm{Mpc}})^2 (\frac{\nu_0}{\mathrm{GHz}})^{-2} (1+z)^{-1} \quad (2)$$

where $S_{\rm CO}$ is the CO integrated intensity, ν_0 is the rest frequency of the CO transition, and z is the redshift. To determine the CO J=3-2/J=1-0 line ratio, we compared the interferometric and single-dish CO J=3-2 data discussed here with published interferometric CO J=1-0 data of similar angular resolution (Downes & Solomon 1998), and single-dish data for Mrk 231 (Solomon et al. 1997) and Mrk 273 (Gao & Solomon 2004). The average single-dish line ratio for the latter two galaxies is 0.48, while the average interferometric line ratio is 0.56, where both values are calculated on the temperature scale. Assuming absolute calibration uncertainties of 20% for both data sets, these two values agree well, and so we adopt an average CO J=3-2/J=1-0 line ratio of 0.5 in calculating the H_2 gas mass. Thus, the H_2 gas mass is calculated via

$$M_{\rm H_2} = 1.6 L'_{\rm CO}(3-2) \tag{3}$$

where $L'_{\rm CO}(3-2)$ is the luminosity of the CO J=3-2 line in K km s^{-1} pc^2. (Note that to obtain the total mass in molecular gas, $M_{\rm mol}$, $M_{\rm H_2}$ would need to be multiplied by a factor of 1.36 to account for helium.) Gas and dust masses and the gas-to-dust mass ratio calculated from the total detected CO J=3-2 and 880 μm luminosity of each galaxy or galaxy component are given in Table 6, while similar quantities calculated from the peak CO J=3-2 emission and 880 μm flux in a single beam are given in Table 7.

3.2. Uncertainties in Gas and Dust Masses

The primary source of uncertainty in the H_2 masses we have calculated is the CO-to-H_2 conversion factor. We have adopted here the value advocated by Downes & Solomon (1998) as being the most appropriate for ultraluminous infrared galaxies. The Milky Way value for this conversion factor is about 5 times larger (Solomon et al. 1997). Thus, if some of the galaxies in our sample, particularly the less luminous ones, have an interstellar medium more similar to that of the Milky Way than that of ultraluminous infrared galaxies, the H_2 masses in Tables 6 and 7 could be underestimated by up to a factor of five. Detailed radiative transfer and dynamical modelling can reduce the uncertainty in this factor by probing the physical conditions directly (Iono et al. 2007) and may provide an independent determination of the CO-to-H_2 conversion factor, and will be presented in a future paper.

A second source of uncertainty comes in our adopted value of the CO J=3-2/J=1-0 line ratio. This uncertainty is probably not as large as the uncertainty caused by the CO-to-H_2 conversion factor, as the line ratio we have adopted as being appropriate for Mrk 231 and Mrk 273 agrees very well with the line ratio seen in star forming regions in more normal spiral galaxies such as M33 (Wilson et al. 1997) and in the more highly inclined galaxies from the sample of Dumke et al. (2001). However, many of the galaxies in the Dumke et al.

(2001) sample have line ratios of 1-1.4, so if it introduces any bias, our adopted line ratio would overestimate the H_2 mass by a factor of at most 2-3. Also, any systematic changes in the line ratio with luminosity or evolutionary phase would introduce similar systematic effects into the gas-to-dust mass ratio. A spatially resolved comparison with high resolution CO J=1-0 images of these galaxies, which would reduce the uncertainty due to the line ratio, will be presented in a future paper (see also Iono et al. 2007).

One major source of uncertainty in the dust masses we have calculated is the dust temperature. An alternative to assuming optically thin dust with emissivity varying as ν^{β} is to assume that the 60 and 100 μm fluxes can be fit with an optically thick blackbody as in Solomon et al. (1997). This method gives, on average, dust temperatures that are 1.5 times larger and dust masses that are 0.55 times smaller than the values given here. The net result of assuming optically thick emission in the far-infrared would be to increase the gas-to-dust mass ratio by about a factor of two. Conversely, if we have overestimated the dust temperature by using single component fits (§3.1), this would have a net effect of decreasing the gas-to-dust mass ratio.

Another source of uncertainty comes from the value of the dust emissivity that we have assumed. A value of $\kappa = 0.9$ cm^2 g^{-1} is appropriate for moderately dense gas in star-forming regions in the Galaxy (Henning et al. 1995; Johnstone et al. 2000), while Dunne et al. (2000) assumed $\kappa = 0.77$ cm^2 g^{-1} (Draine & Lee 1984; Hughes et al. 1993) in deriving dust masses for their survey of nearby galaxies. It is possible that the dust emissivity is modified drastically in the hot, dense central regions of these galaxies. However, without sufficient data at high angular resolution to fit physical dust models (see below), it is impossible at the moment to determine how large an effect this might be. In any case, the dust masses determined here are likely uncertain by a factor of less than 2 due to the uncertain value of κ.

The ideal procedure for determing dust mass would be to fit a detailed physical model to the full infrared spectral energy distribution, as has been done by Galliano et al. (2003) for the dwarf galaxy NGC 1569 or Regan et al. (2004) for NGC 7331. However, only near-infrared and ground-based mid-infrared data can approach the angular resolution of our 880 μm SMA data. The critical mid- and far-infrared spectral regions can be covered by the *Spitzer Space Telescope*, for which the angular resolution ranges from 1.5″ at 3.6 μm to 47″ at 160 μm. Near-infrared data from *Spitzer* can probe the hot dust continuum (Higdon et al. 2006), while data for the mid- and far-infrared part of the spectrum only allow a determination of galaxy-wide dust properties and do not isolate the central regions discussed here. In addition, diffraction-limited ground-based mid-infrared photometry at 12.5 μm is available for nine galaxies in our sample (Soifer et al. 2000, 2001); however, no data beyond 30 μm with arcsecond-scale resolution are currently available from any

instrument. We defer a more detailed analysis of the dust temperature and properties inferred by combining our submillimeter data with infrared data to a future paper.

3.3. Total Gas and Dust Masses from SMA Data

The central H_2 gas masses calculated from the total luminosities detected with the SMA range from 1.4×10^9 $M_\odot$ for NGC 5257 to 1.2×10^{10} $M_\odot$ for NGC 6240 while the central dust masses range from 3×10^6 $M_\odot$ for NGC 1614 to 8×10^7 $M_\odot$ for Mrk 231 (Table 6). The central gas-to-dust ratios also show a wide variation, from as low as 29 for Arp 55(NE) to as high as 720 for NGC 6240. Excluding the three galaxy components with non-detections in the continuum, the average gas-to-dust ratio is 215 ± 53 (rms deviation 207). This value is about 40% larger than the typical Milky Way value of ∼150 (Draine et al. 2007), and there is a large dispersion of the individual values about the average. Our value is also significantly smaller than the value of 540 (rms deviation 290) determined by Sanders et al. (1991) using single-dish CO J=1-0 data and far-infrared luminosities. However, that study adopted a CO-to-H_2 conversion factor that is six times larger than our value, which almost certainly results in an overestimate of the total amount of molecular gas in these galaxies. Adopting the same conversion factor as used in this paper would give a gas-to-dust ratio of 90 for the data in Sanders et al. (1991), somewhat smaller than the ratio obtained here.

The extremely low values seen for Arp 55 and, to some extent, for UGC 5101 and Mrk 231 may be due to a significant contribution to the 880 μm flux from non-thermal or radio free-free emission. However, Arp 55(NE) shows no evidence for a central AGN that could be a source of non-thermal emission (see Appendix). There is some evidence to suggest that UGC 5101 contains a buried AGN (see Appendix), which could increase the 880 μm flux and lead to a small overestimate in the dust mass and an underestimate of the gas-to-dust ratio. Mrk 231 is the one galaxy in our sample for which a dominant AGN contribution has been identified previously at millimeter wavelengths (Downes & Solomon 1998); it is possible that we have underestimated the contribution from the AGN at 880 μm in our calculations. Mrk 273, Arp 299, NGC 6240, and NGC 2623 have all been identified as containing an AGN from X-ray data (Xia et al. 2002; Zezas et al. 2003; Komossa et al. 2003; Maiolino et al. 2003); however, the contribution of non-thermal emission from the AGN at millimeter wavelengths appears to be small (see Appendix).

Extremely high values for the gas-to-dust ratio are measured for NGC 6240, VV 114, and NGC 1614. For NGC 6240, the very broad CO emission line reduces the bandwidth available to measure the continuum flux and produces a large uncertainty in the flux. In addition, the CO J=3-2 emission may be moderately optically thin (Draine et al. 2007),

which could result in the gas mass being overestimated. VV 114 and NGC 1614 are some of the nearest galaxies in our sample and, along with Arp 299, are the only ones for which large amounts of missing flux produce negative bowls in the CO J=3-2 maps. Because these galaxies are relatively nearby, the SMA has greater sensitivity to low surface density gas that is likely to be spatially extended than it would have in some of our more distant galaxies. Figures 15 and 23 show that the CO-emitting regions in these galaxies are quite extended; however, the dust continuum emission does not appear to be significantly extended in these three galaxies. The compact nature of the dust emission suggests that the SMA data are not sufficiently sensitive to pick up continuum emission from dust outside the peak central concentration. In addition, the continuum data suffer slightly more from the missing flux problem than the spectral line data do (§ 2.4 and Tables 4 and 5) because the line emission is intrinsically more compact in an individual spectral channel.

An examination of the relative strengths of the CO J=3-2 emission and the 880 μm emission suggests that this is a reasonable explanation. For example, if the gas-to-dust mass ratio were 150, then, using the equations for dust and gas masses given above, we would expect the flux in the CO J=3-2 moment map to be roughly 10^4 times brighter (in Jy km s^{-1}) than the flux in the 880 μm map (in Jy). For NGC 1614 and Arp 299, if we compare the two maps using contours scaled by this factor of 10^4, we see a very similar extent and relative strength in the CO J=3-2 and 880 μm maps. For VV 114, the central and western peaks are similar in extent and relative strength in the CO J=3-2 and 880 μm maps. However, the eastern peak is fainter in 880 μm continuum than we would expect by a factor of about two, which suggests that either the gas-to-dust ratio or some other property of the gas and dust (such as CO emissivity or temperature) is different in this region.

3.4. Gas and Dust Masses in the Central Kiloparsec

The previous discussion combined with the large range in the gas-to-dust mass ratios seen in Table 6 led us to examine the gas-to-dust ratio using a single resolution element to probe the most central region of each galaxy or galaxy component. For these calculations, we compared the H_2 mass calculated from the integrated CO J=3-2 intensity in a single beam at the peak of the emission with the peak 880 μm continuum intensity (Table 7). Note that since many of the continuum sources are not resolved, the peak continuum emission given in Table 7 has the same value as the integrated flux given in Table 3.

The average gas-to-dust ratio including all 15 galaxies or galaxy components with continuum detections in Table 7 is 120 ± 28 (rms deviation 109). This value is smaller than the average value obtained from the values in Table 6 (i.e., using the total mass detected with

the SMA data) and agrees somewhat better with the typical Milky Way gas-to-dust ratio. Perhaps more importantly, the dispersion about the mean value is smaller by about a factor of two when only the peak values are used, which suggests some of the dispersion seen in the integrated values can be attributed to the better mass sensitivity of the CO observations (see previous section).

Thus our new SMA data suggest that the gas-to-dust mass ratio in the central kiloparsec of these luminous and ultraluminous infrared galaxies is very similar to the gas-to-dust ratio measured in the Milky Way. This result is somewhat surprising given that the dust in these nuclear regions is subject to more intense heating (as well as perhaps processing due to shocks) compared to typical regions in the Milky Way. Perhaps the main zone of activity is very compact and so does not dominate the energetics of the ISM in the entire central kiloparsec; this could be tested by sub-arcsec resolution observations in a direct star formation tracer. Alternatively, perhaps most of the gas and dust reside in high column density clouds or cores that help to shield much of the mass from external heating.

3.5. Possible Variations in Gas and Dust Properties

The normal gas-to-dust ratio seen in these galaxies provides additional validation for the CO-to-H_2 conversion factor derived by Downes & Solomon (1998) and adopted in this analysis. In this section, we check for any systematic differences in the gas-to-dust ratio among the galaxies in our sample that may point to differences in the interstellar medium properties. Our overall picture is one in which the formation and heating of dust tracks the location of molecular gas, regardless of whether that gas is distributed largely in discrete virialized clouds (as in the Galaxy) or to a large extent in a diffuse intracloud medium (as in ULIRGs, where the CO-to-H2 conversion factor is consequently lower). We might expect there to be some differences in our sample, which spans a factor of ten in infrared luminosity and exhibits nuclear separations from less than 1 kpc (if multiple nuclei are seen at all) to 20 kpc. Relatively undisturbed galaxies with a larger nuclear separation are more likely to have a normal interstellar medium with a more normal CO-to-H_2 conversion factor, which would increase the gas mass and the gas-to-dust ratio.

Among the fourteen objects in our sample are five systems in which the two progenitor galaxies can still be clearly distinguished (Arp 299, Arp 55, VV 114, NGC 5331, NGC 5257/8), while the remaining nine objects show a single nucleus or a pair of nuclei separated by less than 1 kpc. If we calculate the gas-to-dust ratio in the central kiloparsec for the extended and the compact galaxies separately, we find no significant difference between the two samples. If we divide the sample as a function of luminosity, we find that the average

gas-to-dust ratio calculated for the lower-luminosity galaxies (160-180 depending on where we divide the sample) is roughly three times larger than the gas-to-dust ratio for the more luminous galaxies (50-70). Thus, there appears to be a strong dependence of the central gas-to-dust ratio on infrared luminosity in our sample, but not on nuclear separation.

These nominally discrepant ratios are in fact compatible with a reasonably uniform gas-to-dust ratio of $\sim 100 - 150$ once plausible corrections are made. We consider here simply changes to the CO-to-H_2 conversion factor, how the dust temperature is derived (optically thick versus optically thin), and the origin of the submillimeter luminosity. We do not consider varying the absolute value of the dust emissivity, κ, since this is relatively poorly constrained in any case. Since the less luminous galaxies show on average good agreement with the Milky Way's gas-to-dust ratio, we focus on possible changes to our analysis that could increase the gas-to-dust ratio in the more luminous galaxies.

One possibility is that the dust temperature is underestimated by our optically thin models and that in fact a higher dust temperature, such as those derived by Solomon et al. (1997), is more appropriate. Using the optically thick dust temperatures would raise the gas-to-dust ratio in these galaxies by about a factor of two. A second possibility is that there is significant non-thermal or free-free emission contaminating the 880 μm flux. This is difficult to quantify but would also act to raise the gas-to-dust ratio. There can be a significant contribution to the far-infrared luminosity from a buried AGN and this contribution can increase with increasing $L_{\rm FIR}$ (Tran et al. 2001). Assuming tha tthe AGN also contributes significant emission at 880 μm, this effect has the right sense to explain the trend of the gas-to-dust ratio with $L_{\rm FIR}$. In contrast, adopting a larger value for the CO-to-H_2 conversion factor (to bring it closer to the value in normal spiral galaxies) would also increase the gas-to-dust ratio, but would not be consistent with previous studies of these extremely luminous galaxies.

4. Correlations between gas and dust properties in the sample

4.1. Testing for correlations

We have searched for correlations among the gas and dust properties in the galaxies in our sample. The physical and observational quantities that were considered were: far-infrared luminosity; dust temperature; the peak H_2 surface density derived from the CO J=3-2 emission; CO J=3-2 beam area; total H_2 gas mass derived from the CO J=3-2 emission detected with the SMA; the ratio of the far-infrared luminosity to the total H_2 mass; the ratio of the far-infrared luminosity to the peak H_2 mass; the peak gas-to-dust mass ratio;

and the CO J=3-2/2-1 line ratio measured from the total flux detected with the SMA. This list includes both physical quantities associated with the star formation and ISM properties as well as properties of the sample (such as beam area and distance) that may introduce selection effects. We note that the CO J=3-2/2-1 line ratio could be underestimated if the SMA maps resolve out a larger fraction of the flux in the higher frequency line. We also note that the peak H_2 surface density may be underestimated in IRAS 17208-0014, which has a bright unresolved core, and also somewhat underestimated in six galaxies (Mrk 231, Mrk 273, IC 694 (Arp 299), Arp 55 NE, Arp 193, and NGC 2623) for which the CO emission is resolved along the long axis but only slightly extended relative to the beam along the short axis of emission. We calculated the correlations using the method described in Akritas & Siebert (1996) to correct for any distance biases in our sample.

We identified eleven correlations that are statistically significant at the 95% confidence level or better ($p \leq 0.05$, where p is the probability of a false correlation after removing the effect of distance; Table 8): far-infrared luminosity and peak H_2 surface density; far-infrared luminosity and dust temperature; dust temperature and peak H_2 surface density; beam area and peak H_2 surface density; CO J=3-2/2-1 line ratio and beam area; CO J=3-2/2-1 line ratio and total H_2 mass detected with the SMA; and the ratio of the far-infrared luminosity to the total H_2 mass detected with the SMA with each of far-infrared luminosity, dust temperature, beam area, CO J=3-2/2-1 line ratio, and the ratio of the far-infrared luminosity to the peak H_2 mass. However, the correlation of surface density with beam area becomes consistent with a null correlation if we use only the twelve galaxies for which the linear resolution of the beam lies between 0.5 and 1.1 kpc, e.g., excluding NGC 5257 and Arp 299. In addition, all five of the correlations with the ratio of the far-infrared luminosity to the total H_2 mass become consistent with a null correlation if we remove NGC 5257 or Arp 299 from the data set. Thus, we conclude that these five correlations are less robust. The remaining five correlations are all significant at the 99% confidence level except for far-infrared luminosity with dust temperature, which is significant at the 98% confidence level; however, this correlation is well known from previous studies with larger samples (Soifer et al. 1989). Plots of these pairs of quantities are shown in Figures 37 and 38.

The correlations of peak H_2 surface density with the far-infrared luminosity and dust temperature suggest that galaxies with higher gas surface densities are more rapidly producing hot young stars, which in turn heat the gas and dust more efficiently. This correlation is consistent with the observed systematic correlation of the HCN luminosity (which traces dense gas mass) with $L_{\rm FIR}$ (Gao & Solomon 2004). The far-infrared luminosity can be used to estimate the star formation rate (Kennicutt 1998), although there can also be a significant contribution from a buried AGN (Tran et al. 2001). Thus, this correlation suggests that higher star formation rates and/or AGN activity are associated with higher gas surface den-

sities inside the central kiloparsec. (Note that this conclusion is somewhat different from the correlation between star formation efficiencies and gas surface densities seen by Scoville et al. (1991) and discussed in § 4.2.) Interestingly, the total H_2 mass detected with the SMA does not correlate with the far-infrared luminosity in our sample, although this may be partly due to the limited range of $L_{\rm FIR}$ in our sample (see Iono et al. (2008) for a discussion of this correlation in the context of a larger sample including high-redshift galaxies.) This lack of correlation suggests that it is the concentration of gas into the central regions that is important for generating the high star formation rates seen in these merging and merger-remnant galaxies, rather than the total amount of fuel available on somewhat larger scales. This result suggests that the increased star formation rate and/or AGN activity inferred for the more luminous infrared galaxies is primarily a result of the increased availability of fuel for star formation in the central kiloparsec.

The CO J=3-2/2-1 line ratio has been used as an indicator of temperature in the molecular gas (Wilson et al. 1997). However, for the galaxies in our sample, there is no obvious correlation between this ratio and the dust temperature derived from the 60 and 100 μm IRAS data. One possible reason for this lack of correlation is that the derived dust temperatures are based on global measurements while the CO J=3-2/2-1 line ratio traces material more concentrated to the center. The line ratio does correlate with both the total molecular gas mass and the beam area (Fig 37). We can think of no obvious physical reason why the line ratio should correlate with the beam area, and so this may be produced by better sensitivity (particularly important for the CO 3-2 line) in the lower resolution data. A similar effect could produce the correlation with total mass, although it could also be hinting at a temperature dependence in the CO-to-H_2 conversion factor, which would affect the derived mass. We do not detect ^{13}CO J=2-1 emission from enough of our galaxies to make similar correlation plots involving this line. We will present an analysis of the various CO line ratios, both integrated and spatially resolved, in combination with radiative transfer models in a future paper.

4.2. Does the central gas surface density correlate with $L_{\rm FIR}/M_{\rm H_2}$?

Scoville et al. (1991) found that the central gas surface density increased as the ratio of far-infrared luminosity to nuclear gas mass increased. The far-infrared luminosity is a good tracer of the star formation rate (Kennicutt 1998); thus, if most of the far-infrared luminosity occurs in the central regions, then this ratio traces the star formation efficiency of the central, high density starburst. Scoville et al. (1991) interpreted the observed trend as indicating that higher star formation efficiencies are produced by higher gas surface densities.

However, our data do not show any evidence of a similar correlation (Figure 39) and so it is worth examining further the possible explanations for the disagreement between these two results.

Scoville et al. (1991) adopted a standard CO-to-H_2 conversion factor and so their gas surface densities can be expected to be a factor of six higher and their infrared luminosity to H_2 mass ratios a factor of six lower than our values. However, this would only shift the absolute scale of their correlation and not change the correlation itself. Indeed, when we estimate their relationship and correct for the different gas masses, we find that it agrees well with the location of most of the points in our analysis (Figure 39). Scoville et al. (1991) used the CO J=1-0 transition in their study, which is more sensitive to cooler, more spatially extended emission than is the CO J=3-2 transition used here. However, by isolating the nuclear emission from any more extended emission, Scoville et al. (1991) may have mitigated the contribution of any extended disk gas in their study.

An additional issue worth considering is the possibility of different sample selection or observational biases. Our galaxy sample spans a slightly smaller range of central gas surface density (a factor of 60) than does the sample in Scoville et al. (1991), which had a range of a factor of 100. However, our range of surface density drops to only a factor of 10 if the galaxy with the poorest spatial resolution (NGC 5257) is removed from the sample. On the other hand, some of the large range in Scoville et al. (1991) may be due to the range of spatial resolution discussed below. The sample in Scoville et al. (1991) has a factor of 10 larger range in $L_{\rm FIR}$ and a factor of 5 larger range in the nuclear or peak gas mass. However, the net result is that the range of $L_{\rm FIR}/M_{\rm H_2}$ (a factor of 10) is similar in the two studies (although the range in our sample drops to a factor of only 4 if we remove NGC 6240). Scoville et al. (1991) calculated this ratio using only the gas mass in the central nuclear source that was also used to calculate the gas surface density, while we have used the peak H_2 mass in the central beam, which would be a difference in the method if many of the sources in the Scoville et al. (1991) sample were spatially resolved. However, most of the sources in the Scoville et al. (1991) sample appear to have been unresolved in the original data sets, which implies that the method used to calculate the surface density and the $L_{\rm FIR}/M_{\rm H_2}$ ratio is very similar in this paper and in Scoville et al. (1991).

Scoville et al. (1991) used CO J=1-0 data for a sample of 14 galaxies, including 5 galaxies from our sample, with resolutions ranging from 0.1 to 3.2 kpc. Although their *range* of resolution is similar to that of the sample presented here, the *distribution* of resolutions is much broader than for our data set, where all but two galaxies (Arp 299 and NGC 5257/8) have resolutions between 0.7 and 1.1 kpc. This distribution of resolutions might introduce systematic effects into the analysis of Scoville et al. (1991) in the sense that galaxies observed

with better angular resolutions could have higher gas surface densities. Indeed, the average resolution for the seven galaxies at the high end of the correlation is 0.66 kpc, while the average resolution for the remaining seven galaxies is 1.14 kpc.

To examine the effect of resolution further, we looked at the five galaxies that are common to both samples (Arp 299/IC694, IRAS 17208-0014, Arp 55, VV 114, and NGC 1614). The values of surface density and $L_{\rm FIR}/M_{\rm H_2}$ ratio are very similar for Arp 299 and NGC 1614, which are two galaxies for which the angular resolutions of the CO J=1-0 and the CO J=3-2 data agree within a factor of two. Both IRAS 17208-0014 and VV 114 move to higher surface densities and $L_{\rm FIR}/M_{\rm H_2}$ ratios using the CO J=3-2 data, which have angular resolutions a factor of 2-3 better than the CO J=1-0 data. The most dramatic change is for Arp 55, for which the CO J=3-2 data have a factor of 8 better angular resolution: its surface density and $L_{\rm FIR}/M_{\rm H_2}$ ratio increase dramatically, to the point where it is larger in both quantities than NGC 1614.

In summary, the better uniformity in angular resolution in our sample compared to that of Scoville et al. (1991) gives us confidence that the lack of correlation seen between the peak H_2 surface density and the ratio of infrared luminosity to H_2 mass seen in our analysis is a real effect and not an artifact of our sample selection or observing techniques. While such a correlation may exist for galaxies with lower far-infrared luminosities (below the luminosity cutoff of our sample), it cannot help us in understanding the high star formation rates in the luminous systems studied here. The data presented here imply a star formation rate (§ 4), not a star formation efficiency, that increases with the central gas surface density. We will explore these interesting correlations further in a future paper.

5. Conclusions

In this paper, we have presented new data obtained with the Submillimeter Array for a sample of fourteen luminous and ultraluminous infrared galaxies selected to have distances $D_L < 200$ Mpc and far-infrared luminosities $\log L_{\rm FIR} > 11.4$. We have obtained data in the CO J=3-2, CO J=2-1, ^{13}CO J=2-1, and HCO^+ J=4-3 lines as well as continuum data at 880 μm and 1.3 mm with spatial resolutions of order 1 kpc or better in all but one of the target galaxies. We present integrated intensity, velocity field, and velocity dispersion maps for the ^{12}CO lines, integrated intensity maps for the continuum, ^{13}CO, and HCO^+ lines, and peak and integrated spectra for all the detected lines.

We have compared our CO J=3-2 and 880 μm continuum fluxes detected with the SMA with published, archival, and new data from the James Clerk Maxwell Telescope. This

comparison shows that the interferometric data miss a significant fraction (typically 50%) of the CO J=3-2 emission for eight of the galaxies in our sample and also a significant fraction (typically 50-80%) of the continuum flux for nine of the galaxies. This large amount of missing continuum flux suggests that a significant fraction of the 880 μm emission in these systems occurs on moderately large spatial scales. The good agreement between the percentage of missing flux seen in the CO J=3-2 line and the 880 μm continuum suggests that the missing continuum flux comes from dust emission associated with molecular gas in the more extended disks of the galaxies.

We have combined our CO and continuum data to determine the gas-to-dust mass ratio in the central regions of these galaxies. We adopt the smaller value of the CO-to-H_2 conversion factor from Downes & Solomon (1998) and calculate the dust temperature by fitting a modified blackbody function as in Klaas et al. (2001). Because of the lower signal-to-noise ratio in the continuum data, we find that we obtain more consistent measurements of the gas-to-dust mass ratio if we use a single beam to probe the central region of each galaxy or galaxy component. We find an average gas-to-dust mass ratio of 120 ± 28 (rms deviation 109), very similar to the value of 150 determined for the Milky Way. This similarity between the gas-to-dust ratio in these luminous systems and that in the Milky Way is somewhat surprising, given that the dust is subject to more intense heating from the starburst and possibly accretion activity compared to typical regions in the Milky Way.

We have searched for correlations among nine physical and observational quantities for the galaxies in our sample. We find five correlations that appear to be statistically significant as well as robust to small changes in the exact galaxy sample. The most interesting correlation is that of peak H_2 surface density with the far-infrared luminosity. Since the far-infrared luminosity can be used to estimate the star formation rate, these correlations suggest that galaxies with higher gas surface densities inside the central kiloparsec have a higher star formation rate. We do not see a significant correlation of total H_2 mass with the far-infrared luminosity, which suggests that the increase in star formation rate is due to the increased availability of molecular gas as fuel for star formation in the central regions, rather than the total amount of gas available on somewhat larger scales.

Our data do not show any evidence of a significant correlation between central gas surface density and the ratio of far-infrared luminosity to nuclear gas mass. This lack of correlation is different from the results of Scoville et al. (1991), who interpreted their observed correlation as indicating that higher star formation efficiencies result from higher gas surface densities. We suggest that the correlation seen by Scoville et al. (1991) was produced by the wider distribution of spatial resolutions in their data set and is not an intrinsic property of these very luminous galaxies. To reiterate, our new data show that it is star formation *rate*,

not star formation *efficiency*, that increases with the central gas surface density in luminous and ultraluminous infrared galaxies

There are a number of additional papers in preparation or planning that will present more detailed analysis of various aspects of the data. We will compare the results from this survey with similar observations of high-redshift submillimeter galaxies to study the gas properties of a wide range of luminous galaxies using the CO J=3-2 line to trace the molecular gas content (Iono et al. 2008). A detailed analysis of the molecular gas properties of NGC 6240 has already been presented in Iono et al. (2007); we will present similar detailed analyses of the gas, dust, and star formation properties individual galaxies such as VV 114 (Petitpas et al. 2008) and Arp 299. We will examine the physical properties of the molecular gas for the entire sample using spatially resolved radiative transfer models, similar to what has been done for NGC6240 (Iono et al. 2007), as well as carry out dynamical analysis and modeling of the galaxies, both of which can give an independent estimate of the CO-to-H_2 conversion factor, similar to the analysis of Downes & Solomon (1998). This physical analysis will also allow us to place constraints on the origin of the OH megamaser activity in luminous infrared galaxies (Darling 2007). We will combine our high-resolution SMA data with *Spitzer* data to compare the properties of the warm and cold dust (see also Armus et al. 2007; Marshall et al. 2007). Finally, we will make detailed comparisons between the molecular gas and dust properties of these U/LIRGs and the predictions of numerical simulations of merging galaxies (e.g., Cox et al. 2006; Chakrabarti et al. 2007).

The Submillimeter Array is a joint project between the Smithsonian Astrophysical Observatory and the Academia Sinica Institute of Astronomy and Astrophysics and is funded by the Smithsonian Institution and the Academia Sinica. The James Clerk Maxwell Telescope is operated by The Joint Astronomy Centre on behalf of the Particle Physics and Astronomy Research Council of the United Kingdom, the Netherlands Organisation for Scientific Research, and the National Research Council of Canada. This research has made use of the NASA/IPAC Extragalactic Database (NED) which is operated by the Jet Propulsion Laboratory, California Institute of Technology, under contract with the National Aeronautics and Space Administration. We are grateful to the many SMA observers who helped to take the data presented in this paper and to the SMA TAC for giving this project a high priority. We thank James di Francesco for making available to us the pipeline processed archival SCUBA data for VV 114, NGC 5331, and Arp 299, Padelis Papadopoulos for access to his single dish CO data, and the anonymous referee for a very useful and prompt referee report. C.D.W. and J.G. acknowledge support by the Natural Science and Engineering Research Council of Canada (NSERC). A.J.B. acknowledges support by National Science Foundation grant AST-0708653. M.J. acknowledges support by the Academy of Finland grant 124620.

Facilities: SMA, JCMT.

A. Discussion of individual galaxies

A.1. IRAS 17208-0014

Veilleux et al. (1995) classify the optical spectrum of IRAS 17208-0014 as HII. High-resolution near-infrared imaging shows no direct evidence of an AGN, as the nuclear emission is extended in all bands (Scoville et al. 2000). The [NeV] line, which is an indicator of an AGN, is not detected in this galaxy (Farrah et al. 2007). High-resolution radio imaging at 4.8 GHz also shows no evidence for an AGN (Baan & Klöckner 2006). Near-infrared images show extended emission with a brighter nucleus (Scoville et al. 2000).

However, the millimeter continuum fluxes in Table 3 suggest there may be a significant non-thermal or free-free component present. The 880 μm and 1.4 mm continuum fluxes are inconsistent with dust with $\beta = 1.5$ at greater than the 1.5σ level even after including 20% calibration uncertainties. If we assume that any nonthermal component depends inversely on frequency (Condon 1992) while the dust component varies as $\nu^{3.5}$ (dust emissivity $\beta = 1.5$), then the non-thermal emission would contribute 40% of the flux at 880 μm.

A.2. Mrk 231 (UGC 8058, VII Zw 490)

Mrk 231 is the only object in our sample to show strong emission from an AGN. Veilleux et al. (1995) classify the optical spectrum as Seyfert 2, while Genzel et al. (1998) suggest an AGN-like radiation field based on mid-infrared emission lines and limits. Smith et al. (1998) suggest an AGN based on their 22 GHz VLA data; Lonsdale et al. (2003) find that VLBI imaging data are most consistent with an AGN morphology, although they point out that the AGN may not be responsible for the majority of the bolometric luminosity of the galaxy. However, Davies et al. (2004) find that the nuclear starburst contributes 25-40% of the bolometric luminosity. Mrk 231 also contains a hard X-ray source that is variable on timescales of a few hours (Gallagher et al. 2002).

The millimeter continuum fluxes in Table 3 suggest there is a significant non-thermal component present. Downes & Solomon (1998) attributed all but 20% of their 1.3 mm continuum flux to non-thermal emission. If we assume that any nonthermal component depends inversely on frequency (Condon 1992) while the dust component varies as $\nu^{3.5}$ (dust emissivity $\beta = 1.5$), then the non-thermal emission contributes perhaps 25% of the flux at

880 μm.

A.3. Mrk 273 (UGC 8696, VV 851, I Zw 71)

Veilleux et al. (1995) classify the optical spectrum of Mrk 273 as LINER. Genzel et al. (1998) suggest that the mid-infrared radiation has equal contributions from a starburst and an AGN. Armus et al. (2007) detect both [NeV] emission and continuum emission from dust hotter than 300 K, both of which indicate the presence of an AGN. Xia et al. (2002) detect hard X-ray emission from the northern nucleus, while Ptak et al. (2003) detect the Fe line in X-rays, both suggesting the presence of an AGN. However, Smith et al. (1998) find that the compact 22 GHz core can be fit by a model of clustered supernovae. Near-infrared images show extended emission with two bright central sources (Scoville et al. 2000).

The relative strength of the 1.3 and 2.6 mm continuum emission (Downes & Solomon 1998) suggests that some non-thermal emission is present. However, the contribution at 880 μm would be small and well within the 20% calibration uncertainty of the data.

A.4. IRAS 10565+2448

This galaxy has been relatively poorly studied. Veilleux et al. (1995) classify the optical spectrum of IRAS 10565+2448 as HII. Condon et al. (1991) do not find any compact radio continuum peak at 1.49 GHz. Near-infrared images show extended emission with a brighter nucleus (Scoville et al. 2000). The [NeV] line, which is an indicator of an AGN, is not detected in this galaxy (Farrah et al. 2007).

The millimeter continuum data are consistent with pure dust emission, although the 1.3 mm continuum point is on the large side of what is possible, leaving open the possibility of a small non-thermal contribution at 880 μm.

A.5. UGC 5101

Veilleux et al. (1995) classify the optical spectrum of UGC 5101 as LINER. Although Genzel et al. (1998) suggest the mid-infrared radiation field is more similar to that of a starburst than an AGN, Armus et al. (2004) find that [NeV] emission implies this source contains a buried AGN. Armus et al. (2007) detect continuum emission from dust hotter than 300 K, which also indicates the presence of an AGN. Imanishi et al. (2003) detect hard

X-ray emission, including the Fe line, which they interpret as evidence for a buried AGN. Lonsdale et al. (2003) use VLBI imaging to find that an AGN is responsible for at least 10% of the total radio flux. Near-infrared images show extended emission with a brighter nucleus (Scoville et al. 2000).

The millimeter continuum data are consistent with pure dust emission, although the 1.3 mm continuum point is on the large side of what is possible, leaving open the possibility of a small non-thermal contribution at 880 μm.

A.6. Arp 299 (VV 118, NGC 3690, Mrk 171, IC 694)

High-resolution radio images from 1.4 to 8.4 GHz reveal five bright compact sources as well as extended emission (Neff et al. 2004). The bright compact radio source in the nucleus of IC 694 breaks up into five candidate radio supernova remnants when observed with the VLBA; one of the sources may possibly be a low-luminosity AGN (Neff et al. 2004). X-ray images reveal a population of compact sources, including sources in the nucleus of each component which are likely to be AGN (Zezas et al. 2003). Further evidence for an AGN in NGC 3690 comes from García-Marín et al. (2006), who identify a conical region with Seyfert-like excitation emanating from the B1 region. Mid-infrared images show three compact sources associated with the two nuclei as well as the emission region north of NGC 3690 (Soifer et al. 2001); near-infrared images reveal a fourth compact source near NGC3690 as well as extended emission (Alonso-Herrero et al. 2000)

The combination of the 2.6 mm continuum flux from Aalto et al. (1997) with the 1.3 mm continuum flux from this paper suggests that some non-thermal component may be present in the eastern component (IC694). If we assume the non-thermal emission scales inversely with frequency and that all of the 2.6 mm continuum emission is non-thermal, then any non-thermal contribution at 880 μm would be less than 10% of the total.

A.7. Arp 55 (UGC 4881, VV 155)

Arp 55 is one of the least studied galaxies in our sample. Veilleux et al. (1995) classify the optical spectrum as HII for both components. Lonsdale et al. (1993) detected Arp 55 using VLBI observations, but find the source to be consistent with a compact starburst or a group of clustered supernova.

A.8. Arp 193 (IC 883, VV 821, UGC 8387, I Zw 56)

Veilleux et al. (1995) classify the optical spectrum as LINER. 8.4 GHz images from the VLA show disk-like extended emission with no sign of a compact source (Condon et al. 1991). Rush et al. (1996) give an upper limit on the soft X-ray luminosity. Near and mid-infrared images also show disk-like extended emission (Scoville et al. 2000; Soifer et al. 2001).

A.9. NGC 6240 (IC 4625, UGC 10592, VV 617)

Veilleux et al. (1995) classify the optical spectrum as LINER. However, hard X-ray imaging has revealed two AGNs separated by $\sim 1''$ (Komossa et al. 2003). Armus et al. (2007) detect continuum emission from dust hotter than 300 K, which also indicates the presence of an AGN. High-resolution radio images from 2.3 to 8.4 GHz reveal two compact radio sources with properties similar to Seyfert nuclei (Gallimore & Beswick 2004). Near-infrared images also show two nuclei as well as bright extended emission (Scoville et al. 2000). For a more complete discussion of the multi-wavelength properties of NGC 6240, see Iono et al. (2007).

A.10. VV 114 (Arp 236, IC 1623)

Veilleux et al. (1995) classify the optical spectrum as HII for both components. 8.4 GHz images from the VLA show no sign of a compact source (Condon et al. 1991). However, Le Floc'h et al. (2002) find that the mid-infrared spectrum shows signs of an AGN in the eastern component. Near and mid-infrared images show extended emission in both components with a bright compact source in the eastern component (Scoville et al. 2000; Soifer et al. 2001).

The millimeter continuum data are consistent with pure dust emission, although the 1.3 mm continuum point for IC694 is on the large side of what is possible, leaving open the possibility of a small non-thermal contribution at 880 μm.

A.11. NGC 5331 (UGC 8774, VV 253)

This galaxy has been relatively poorly studied. Ashby et al. (1995) classify both components as starbursts based on optical spectroscopy and Rush et al. (1996) give an upper limit on the soft X-ray luminosity. Condon et al. (1990) detect both components at 1.49

GHz, with the southern component being about twice as strong as the northern component.

A.12. NGC 2623 (Arp 243, UGC 4509)

Heckman et al. (1983) classify the optical spectrum as LINER. 8.4 GHz images from the VLA show a strong compact radio source (Condon et al. 1991). Maiolino et al. (2003) classified this galaxy as an obscured AGN using X-ray observations from Chandra. Near and mid-infrared images show a single compact nucleus (Scoville et al. 2000; Soifer et al. 2001).

The combination of the 1.3 mm continuum flux from Table 3 with the 880 μm continuum flux from this paper suggests that some small non-thermal component may be present. If we assume the non-thermal emission scales inversely with frequency and that the dust emissivity goes as $\beta = 1.5$, then any non-thermal contribution at 880 μm would be less than 10% of the total.

A.13. NGC 5257, NGC 5258 (Arp 240, VV 55, UGC 8641, UGC 8645)

Veilleux et al. (1995) classify the optical spectrum as HII and Rush et al. (1996) give an upper limit on the soft X-ray luminosity of NGC5258. 8.4 GHz images from the VLA show emission in both components that is somewhat extended (Condon et al. 1991). Smith et al. (2007) present Spitzer mid-infrared images at 3.6, 8, and 24 μm, which show that the bright arm seen in CO in NGC5258 is also prominent at 24 μm.

NGC 5258 is an unusual case in that most of the CO J=3-2 emission seen by the SMA comes from the bright southern arm, with only weak emission seen from the nucleus. Surprisingly, this galaxy contains the strongest continuum source in our entire sample and is detected at the 6σ level despite a relatively high noise in the SMA image. However, this point source is not located at the center of the galaxy but rather (-15,8) arcseconds to the north-west. Thus, the low gas-to-dust ratio seen in Table 6 is most likely spurious.

A.14. NGC 1614 (Arp 186, Mrk 617)

Veilleux et al. (1995) classify the optical spectrum of NGC 1614 as HII, although the [NII] lines suggest a LINER classification. Neff et al. (1990) find no direct evidence for an AGN component in their 4.6 GHz maps. Fritz et al. (2006) fit the infrared spectral energy distribution with a type II AGN model; however, these model fits suggest that starburst

emission is likely the dominant component at 880 μm. High-resolution radio, near-infrared, and mid-infrared imaging reveal a starforming ring with diameter 1.2″ (Soifer et al. 2001; Alonso-Herrero et al. 2001; Neff et al. 1990).

NGC 1614 is the only object in our sample besides Mrk 231 to show clear evidence of a non-thermal component from the ratio of its millimeter continuum fluxes. The peak 880 μm and 1.3 mm continuum fluxes are almost identical (Tables 3 and 7). If we assume that any non-thermal component depends inversely on frequency, then dust emission represents perhaps 60% of the total 880 μm flux and only 40% of the peak 880 μm flux. However, correcting for this putative non-thermal component produces the highest peak gas-to-dust ratio of any galaxy in our sample (Table 7).

REFERENCES

Ashby, M. L. N., Houck, J. R., & Matthews, K. 1995, ApJ, 447, 545

Aalto, S., Radford, S. J. E., Scoville, N. Z., & Sargent, A. I. 1997, ApJ, 475, L107

Akritas, M. G., & Siebert, J., 1996, MNRAS, 278, 919

Alonso-Herrero, A., Rieke, G. H., Rieke, M. J., & Scoville, N. Z., 2000, ApJ, 532, 845

Alonso-Herrero, A., Engelbracht, C. W., Rieke, M. J., Rieke, G. H., & Quillen, A. C. 2001, ApJ, 546, 952

Aretxaga, I., Hughes, D. H., Chapin, E. L., Gazta naga, E., Dunlop, J. S., & Ivison, R. J., 2003, MNRAS, 342, 759

Aretxaga, I., Hughes, D. H., & Dunlop, J. S., 2005, MNRAS, 358, 1240

Armus, L. et al., 2004, ApJS, 154, 178

Armus, L. et al., 2007, ApJ, 656, 148

Baan, W. A., & Klöckner, H.-R. 2006, A&A, 449, 559

Blain, A. W., Smail, I., Ivison, R. J., Kneib, J.-P., & Frayer, D. T. 2002, Physics Reports, 369, 111

Braine, J., Lisenfeld, U., Duc, P.-A., et al. 2004, A&A, 418, 419

Bryant, P. M. & Scoville, N. Z. 1996, ApJ, 457,, 678

Bryant, P. M. & Scoville, N. Z. 1999, AJ, 117, 2632

Carico, D. P., Keene, J., Soifer, B. T., & Neugebauer, G. 1992, PASP, 104, 1086

Chakrabarti, S., Cox, T. J., Hernquist, L., Hopkins, P. F., Robertson, B., & Di Matteo, T., 2007, ApJ, 658, 840

Condon, J. J., Huang, Z.-P., Yin, Q. F., & Thuan, T. X. 1991, ApJ, 378, 65

Condon, J. J., Helou, G., Sanders, D. B., Soifer, B. T., 1990, ApJS, 73, 359

Condon, J. J. 1992, ARA&A, 30, 575

Conselice, C. J., Chapman, S. C., & Windhorst, R. A. 2003, ApJ, 596, L5

Cox, T. J., Primack, J., Jonsson, P., & Somerville, R. S., 2004, ApJ, 607, L87

Cox, T. J., Dutta, S. N., Di Matteo, T., Hernquist, L., Hopkins, P. F., Robertson, B., & Springel, V., 2006, ApJ, 650, 791

Dame, T. M., Hartmann, D., & Thaddeus, P. 2001, ApJ, 547, 792

Darling, J., 2007, ApJ, 572, 810

Darling, J. & Giovanelli, R. 2002, ApJ, 669, L9

Dasyra, K. M., et al., 2006, ApJ, 651, 835

Davies, R. I., Tacconi, L. J., & Genzel, R., 2004, ApJ, 613, 781

Di Francesco, J., Johnstone, D., Kirk, H., MacKenzie, T., & Ledwosinska, E., 2008, ApJS, 175, 277

Downes, D., & Solomon, P.M. 1998, ApJ, 507, 615

Draine, B. T., & Lee, H. M., 1984, ApJ, 285, 89

Draine, B. T., Dale, D. A, Bendo, G., et al., 2007, ApJ, 663, 866

Dumke, M., Nieten, Ch., Thuma, G., Wielebinski, R., & Walsh, W., 2001, A&A, 373, 853

Dunne, L., Eales, S., Edmunds, M., Ivison, R., Alexander, P., & Clements, D. L. 2000, MNRAS, 315, 115

Farrah, D. et al., 2007, ApJ, 667, 149

Frayer, D. T., Ivison, R. J., Scoville, N. Z., et al. 1998, ApJ, 506, L7

Frayer, D. T., Ivison, R. J., Scoville, N. Z., et al. 1999, ApJ, 514, L13

Fritz, J., Franceschini, A., & Hatziminaoglou, E. 2006, MNRAS, 366, 767

Gallagher, S. C., Brandt, W. N., Chartas, G., Barmire, G. P., & Sambruna, R. M. 2002, ApJ, 569, 655

Galliano, F., Madden, S. C., Jones, A. P., Wilson, C. D., Bernard, J.-P., & Le Peintre, F. 2003, A&A, 407, 159

Gallimore, J. F., & Beswick, R., 2004, AJ, 127, 239

Gao, Y. & Solomon, P. M. 2004, ApJS, 152, 63

García-Marín, M., Colina, L., Arribas, S., Alonso-Herrero, A., & Mediavilla, E., 2006, ApJ, 650, 850

Genzel, R. et al. 1998, ApJ, 498, 579

Goldreich, P. & Kwan, J., 1974, ApJ, 189, 441

Greve, T. R., Bertoldi, F., Smail, I., et al. 2005, MNRAS, 359, 1165

Graciá-Carpio, J., García-Burillo, S., Planesas, P., & Colina, L., 2006, ApJ, 640, L135

Greve, T. R., Papadopoulos, P. P., Gao, Y., & Radford, S. J. E., 2007, ApJ, submitted (astro-ph/0610378)

Gottlöber, S., Klypin, A., & Kravtsov, A. V. 2001, ApJ, 546, 223

Heckman, T. M., van Breugel, W., Miley, G. K., & Butcher, H. R., 1983, AJ, 88, 1077

Henning, Th., Michel, B., & Stignienko, R. 1995, Planet. Space Sci., 43, 1333

Higdon, S. J. U., Armus, L., Higdon, J. L., Soifer, B. T., & Spoon, H. W. W. 2006, ApJ, 648, 339

Hinz, J. L. & Rieke, G. H., 2006, ApJ, 646, 872

Ho, P. T. P., Moran, J. M., & Lo, K. Y., 2004, ApJ, 616, L1

Hughes, D. H., et al., 1993, MNRAS, 263, 607

Imanishi, M., Terashima, Y., Anabuki, N., & Nakagawa, T. 2003, ApJ, 596, L167

Imanishi, M. & Nakanishi, K., 2006, PASJ, 58, 813

Imanishi, M., Nakanishi, K., Tamura, Y., Oi, N., & Kohno, K., 2007, AJ, 134, 2366

Iono, D. et al. 2004, ApJ, 616, L63

Iono, D., Yun, M. S., & Ho, P. T. P. 2005, ApJS, 158, 1

Iono, D., Wilson, C., Takakuwa, S., Yun, M. S., Petitpas, G. R., Peck, A. B., Ho, P. T. P., Matsushita, S., Pihlstrom, Y. M., & Wang Z., 2007, ApJ, 659, 283

Iono, D. et al., 2008, submitted to ApJ

Johnstone, D., Wilson, C. D., Moriarty-Schieven, G., Joncas, G., Smith, G., & Fich, M. 2000, ApJ, 545, 327

Juvela, M. 1997, A&A, 322, 943

Juvela, M. & Padoan P., 2003, A&A, 397, 201

Kennicutt, R. C., 1998, ARA&A, 36, 189

Klaas, U. et al. 2001, A&A, 379, 823

Komossa, S., Burwitz, V., Hasinger, G., Predehl, P., & Kaastra, J. S.; Ikebe, Y., 2003, ApJ, 582, L15

Le Fèvre, O., Abraham, R., Lilly, S. J., et al. 2000, MNRAS, 311, 565

Le Floc'h, E., Charmandaris, V., Laurent, O., Mirabel, I. F., Gallais, P., Sauvage, M., Vigroux, L., & Cesarsky, C. 2002, A&A, 391, 417

Lonsdale, C. J., Smith, H. J., & Lonsdale, C. J. 1993, ApJ, 405, L9

Lonsdale, C. J., Lonsdale, C. J., Smith, H. E., & Diamond, P. J. 2003, ApJ, 592, 804

Maiolino, R., et al. 2003, MNRAS, 344, L59

Marshall, J. A., Herter, T. L., Armus, L., Charmandaris, V., Spoon, H. W. W., Bernard-Salas, J., & Houck, J. R. 2007, ApJ, 670, 129

Meier, D. S., & Turner, J. L., 2001, ApJ, 551, 687

Mihos, J. C. & Hernquist, L. 1996, ApJ, 464, 641

Mundell, C. G., Ferruit, P. & Pedlar, A., 2001, ApJ, 560, 168

Murphy, T. W., Jr., Armus, L., Matthews, K., et al. 1996, AJ, 111, 1025

Murphy, T. W., Jr., Soifer, B. T., Matthews, K., & Armus, L. 2001, ApJ, 559, 201

Neff, S. G., Hutchings, J. B., Stanford, S. A., & Unger, S. W. 1990, AJ, 99, 1088

Neff, S. G., Ulvestad, J. S., & Teng, S. H., 2004, ApJ, 611, 186

Neri, R. et al. 2003, ApJ, 597, L113

Papadopoulos, P. P., 2007, ApJ, 656, 792

Petitpas, G. R., et al. 2008, in preparation.

Ptak, A., Heckman, T., Levenson, N. A., Weaver, K., & Strickland, D. 2003, ApJ, 592, 782

Regan, M. W. et al. 2004, ApJS, 154, 204

Rigopoulou, D., Lawrence, A., & Rowan-Robinson, M. 1996, MNRAS, 278, 1049

Rosolowsky, E. W., Plambeck, R., Engargiola, G., & Blitz, L. 2003, ApJ, 599, 258

Rush, B., Malkan, M. A., Fink, H. H., & Voges, W., 1996, ApJ, 471, 190

Sakamoto, K., Scoville, N. Z., Yun, M. S., Crosas, M., Genzel, R., & Tacconi, L. J. 1999, ApJ, 514, 68

Sakamoto, K., Ho,. P. T. P., Iono, D. et al., 2006, ApJ, 636, 685

Sanders, D. B., Soifer, B. T., Elias, J. H., Madore, B. F., Matthews, K., Neugebauer, G., & Scoville, N. Z. 1988, ApJ, 325, 74

Sanders, D. B., Soifer, B. T., Scoville, N. Z., & Sargent, A. I., 1988, ApJ, 324, L55

Sanders, D. B., Scoville, N.Z., & Soifer, B. T., 1991, ApJ, 370, 158

Sanders, D. B. & Mirabel, I. F., 1996, ARA&A, 34, 739

Sanders, D. B., Mazzarella, J. M., Kim, D.-C., Surace, J. A., & Soifer, B. T. 2003, AJ, 126, 1607

Sault, R. J., Teuben, P. J., & Write, M. C. H., 1995, ASPC, 77, 433

Scoville, N. Z. & Solomon, P. M. 1974, ApJ, 187, L67

Scoville, N. Z., Sanders, D. B., Sargent, A. I., Soifer, B. T., & Tinney, C. G. 1989, ApJ, 345, L25

Scoville, N. Z., Sargent, A. I., Sanders, D. B., & Soifer, B. T., 1991, ApJ, 366, L5

Scoville, N. Z. et al. 2000, AJ, 119, 991

Seaquist, E. R., Yao, L., Dunne, L., & Cameron, H, 2004, MNRAS, 349, 1428

Smith, B. J., Struck, C., Hancock, M., Appleton, P. N., Charmandaris, V. & Reach, W. T., 2007, AJ, 133, 791

Smith, H. E., Lonsdale, C. J., & Lonsdale, C. J. 1998, ApJ, 492, 137

Soifer, B. T., Boehmer, L., Neugebauer, G., & Sanders, D. B., 1989, AJ, 98, 766

Solomon, P. M., Downes, D., Radford, S. J. E., & Barrett, J. W. 1997, ApJ, 478, 144

Soifer, B. T., et al., 2000, AJ, 119, 509

Soifer, B. T., et al., 2001, AJ, 122, 1213

Strong, A. W. et al. 1988, A&A, 207, 1

Strong, A. W. & Mattox, J. R. 1996, A&A, 308, L21

Tacconi, L., Genzel, R., Tecza, M., Gallimore, J. F., Downes, D., & Scoville, N. Z. 1999, ApJ, 524, 732

Tacconi, L. et al., 2006, ApJ, 640, 228

Tran, Q. D., et al. 2001, ApJ, 552, 527

Veilleux, S., Kim, D.-C., Sanders, D. B., Mazzarella, J. M., & Soifer, B. T. 1995, ApJS, 98, 171

Veilleux, S., Kim, D.-C., & Sanders, D. B. 2002, ApJS, 143, 315

Wang, J. et al. 2004, ApJ, 616, L67

Wilson, C. D. & Scoville, N. Z. 1990, ApJ, 363, 435

Wilson, C. D., Walker, C. E., & Thornley, M. D. 1997, ApJ, 483, 210

Xia, Y. Y., Xue, S. J., Mao, S., Boller, Th., Deng, Z. G., & Wu, H. 2002, ApJ, 564, 196

Yang, M. & Phillips, T., 2007, ApJ, 662, 284.

Yao, L., Seaquist, E. R., Kuno, N., & Dunne, L. 2003, ApJ, 588, 771

Young, J. S., Schloerb, F. P., Kenney, J. D., & Lord, S. D. 1986, ApJ, 304, 443

Young, J. S., Xie, S., Kenney, J. D., & Rice, W. L. 1989, ApJS, 70, 699

Yun, M. S. & Carilli, C. R. 2002, ApJ, 568, 88

Yun, M. S., Scoville, N. Z., & Knop, R. A. 1994, ApJ, 430, L109

Zezas, A., Ward, M. J., & Murray, S. S., 2003, ApJ, 594, L31

Table 1. **The Nearby Luminous Infrared Galaxy Sample**

Galaxy	$\log L_{\rm FIR}$ ($L_\odot$)	D_L (Mpc)	cz
IRAS 17208-0014	12.41	189	12835
Mrk 231	12.31	179	12642
Mrk 273	12.08	166	11327
IRAS 10565+2448	11.93	191	12921
UGC 5101	11.87	174	11809
Arp 299	11.74	44	3088
Arp 55	11.60	173	11900
Arp 193	11.59	102	7000
NGC 6240	11.54	107	7339
VV 114	11.50	87	6010
NGC 5331	11.49	145	9907
NGC 2623	11.48	80	5535
NGC 5257/8	11.43	99	6775
NGC 1614	11.43	69	4778

Table 2. **Observational Properties of the Survey**

	CO J=3-2 Observations				CO J=2-1 Observations			
Galaxy	Date Observed	Number of Antennas	Sensitivity[a] (mJy (K))	Time (hr)	Date Observed	Number of Antennas	Sensitivity[a] (mJy (K))	Time (hr)
IRAS 17208-0014	20050818,0516	6	86 (1.01)	5.9	...	...	...	...
Mrk 231	20060205	8	33 (0.55)	3.3	...	...	...	...
Mrk 273	20060204	7	45 (0.67)	3.8	...	...	...	...
IRAS 10565+2448	20060202	7	25 (0.46)	3.7	20060206	7	15 (0.36)	4.8
UGC 5101	20060130	6	32 (0.56)	5.6	20060207	7	18 (0.39)	5.0
Arp 299	20060410	7	37 (0.087)	5.6	20070327	8	20 (0.086)	6.6
Arp 55	20060129	6	40 (0.74)	4.3	20060211	7	18 (0.44)	6.3
Arp 193	20060416	8	38 (0.093)	3.6	...	...	...	...
NGC 6240	20051009,1014	7	44 (0.24)	9.9	...	...	...	...
VV 114	051113	7	31 (0.057)	4.4	20051115,1125	7	15 (0.029)	7.0
NGC 5331	20070325	8	50 (0.23)	6.3	20060422	8	21 (0.047)	5.0
NGC 2623	20070116	8	12 (0.028)	6.7	20060212,0213,0313	6,8	20 (0.40)	13.0
NGC 5257/8	...	...	...	...	20060318	8	51 (0.12)	4.8
NGC 5257	20060411,20070502	7,6	127 (0.12)	3.0	...	...	...	...
NGC 5258	20060411,20070502	7,6	165 (0.16)	3.0	...	...	...	...
NGC 1614	20051114	7	41 (0.079)	5.1	20051112	7	14 (0.027)	5.5

[a]Noise level measured from the dirty map using line-free channels with 20 km s^{-1} resolution.

Table 3. **Interferometric CO and continuum fluxes**

Galaxy	CO J=3-2 flux (Jy km s^{-1})	beam ($''$)	880 μm[a] (mJy)	HCO^+ J=4-3 flux[b] (Jy km s^{-1})	CO J=2-1 flux (Jy km s^{-1})	^{13}CO J=2-1 flux[a] (Jy km s^{-1})	1.4mm[a] (mJy)	beam ($''$)	CO J=1-0 flux (Jy km s^{-1})	3mm (mJy)	beam ($''$)	Refs.[c]
IRAS 17208-0014	478 ± 33	1.0x0.9	48 ± 10	...	355 ± 7	...	37 ±3	1.0x0.7	132	<5	5.1x1.6	1,10
Mrk 231	308±8	0.9x0.8	80±4	25±3	280	...	36	0.7x0.5	97	63	1.3x1.1	1
Mrk 273	441± 14	0.9x0.8	56±5	...	231	...	8	0.6	78	11	1.4x1.3	1
IRAS 10565+2448	204±7	0.9x0.7	15±3	...	187 ± 6	< 2	6 ± 1	1.1x1.0	68	< 2	2.3x1.4	1
UGC 5101	209±10	1.0x0.7	37±9	...	237 ± 10	< 4	12 ± 2	1.2x0.9	50	...	2.1x1.6	2
Arp 299	2582±34	2.3x1.9	101±7	≥67 ± 5	1976 ± 16	38.8 ± 3.4	46 ± 6	3.1x1.8	397	31±3	2.5x2.2	3
... IC 694	≥ 1610± 27	"	81±5	≥50 ± 4	1168 ± 13	17.5 ± 2.7	40 ± 6	"	242	17±2	"	3
... NGC3690	≥ 596± 17	"	20±5	≥17 ± 3	355 ± 8	3.5 ± 1.1	<4	"	53	5±2	"	3
Arp 55	146±12	0.9x0.8	26±7	...	163 ± 9	< 6	< 2	1.1x0.9	83	...	9x7	4
... Arp 55(NE)	94±9	0.9x0.8	26±7	...	110 ± 8	< 3	< 2	"	...	...	"	4
... Arp 55(SW)	52±8	0.9x0.8	< 8	...	53 ± 4	< 3	< 2	"	...	...	"	4
Arp 193	886 ± 15	2.2x2.0	39 ± 4	≥21 ± 5	450	...	10	0.6x0.4	161	<5	1.3x0.9	1
NGC 6240	2428 ± 52	1.6x1.3	33 ± 13	≥166 ± 12	1220	...	5.9 ± 0.3	0.9x0.5	324	...	4.9x4.1	7,9
...NGC 6240(central)	2318 ± 48	1.6x1.3	33 ± 13	≥166 ± 12	1220	...	5.9 ± 0.3	0.9x0.5	324	...	4.9x4.1	7,9
...NGC 6240(WC)	110 ± 19	1.6x1.3	<16	...	...	...	...	...	...	...	...	7,9
VV 114	1530 ± 16	2.8x2.0	26 ± 6	≥17 ± 2	1109 ± 8	10.6 ± 2.6[d]	11 ± 2	4.1x3.0	674	<16	4.4x3.1	5
NGC 5331	478 ± 26	2.3x1.0	27 ± 6	...	333 ± 11	8.8 ± 2.4	8 ± 2	3.5x3.1	167	...	5.4x4.4	6
... NGC 5331S	401 ± 24	"	27 ± 6	...	250 ± 7	8.8 ± 2.4	8± 2	"	150	...	"	6
... NGC 5331N	77 ± 10	"	< 12	...	83 ± 9	< 4	< 4	"	17	...	"	6
NGC 2623	607 ± 5	2.2x2.0	50 ± 2	27 ± 2	267 ± 8	< 3	17 ± 3	1.2x1.0	153	...	3.5x2.4	7
NGC 5257/8	1140 ± 70	3.8x3.0	104 ± 21	...	344 ± 51	< 20	< 16	3.5x2.8	387	...	6.2x3.7	6
... NGC 5257	286 ± 47	"	< 26	...	109 ± 24	< 10	< 8	"	137	...	"	6
... NGC 5258	854 ± 52	"	104 ± 21[e]	...	235 ± 45	< 10	< 8	"	250	...	"	6
NGC 1614	674 ± 14	2.6x2.1	27 ± 7	≥14 ± 3	670 ± 7	17.3 ± 2.7	21 ± 3	3.7x3.3	215	...	4x6	8

[a]Upper limits are 2σ in a single beam (per galaxy component, if applicable).

[b]ower limits indicated that the HCO^+ J=4-3 flux of the galaxy is uncertain because the full width of the line may not be contained within the spectrometer; see text.

[c]References are for CO J=1-0 and 3 mm properties; for Mrk 231, Mrk 273, Arp 193, and NGC 6240, reference is also for CO J=2-1 and 1.3 mm properties. 1. Downes & Solomon (1998). 2. Genzel et al. (1998). 3. Aalto et al. (1997). 4. Sanders et al. (1988b). 5. Yun et al. (1994). 6. Iono et al. (2005). 7.Bryant & Scoville (1999). 8. Scoville et al. (1989). 9. Tacconi et al. (1999) 10. L. Tacconi & A. Baker, private communication.

[d]Only the eastern peak of VV 114 is detected in the ^{13}CO J=2-1 line.

[e]NGC 5258 contains an off-nuclear continuum source whose flux is quoted here. The nucleus is undetected at < 30 mJy (2σ).

Table 4. **CO 3-2 single dish and interferometric fluxes**

Galaxy	CO3-2(SMA) (Jy km s^{-1})	CO3-2(JCMT)[a] (Jy km s^{-1})	Missing flux[b] (Jy km s^{-1})	Percent missing flux[b]
IRAS 17208-0014	478 ± 33	985 ± 128	510 ± 260	(51 ± 15)%
Mrk 231	308±8	480±100	170±150	(35±23)%
Mrk 273	441± 14	410±90	0	0
IRAS 10565+2448	204±7	470±60	270±120	(57±14)%
UGC 5101	209±10	490±80	280±130	(57±14)%
Arp 299	2582 ± 57	4890±180[e]	2300 ± 1600	(47 ± 19)%
Arp 55	146 ±9	$\geq$ 425 ± 40[c]	$\geq$ 280 ± 100	($\geq$ 66 ± 10)%
Arp 193	890 ± 15	1118 ± 94	230 ± 300	(20 ± 24)%
NGC 6240	2428 ± 52	3205 ± 642	780 ± 1030	(24 ± 26)%
VV 114	1530 ± 16	2956 ± 133[d]	1430 ± 680	(48 ± 15)%
NGC 5331S	401 ± 24	...	...	...
NGC 5331N	77 ± 10	...	...	...
NGC 2623	607 ± 5	620 ± 44[d]	13 ± 190	(2 ± 29)%
NGC 5257	286 ± 47	437 ± 67	151 ± 133	(36 ± 24)%
NGC 5258	854 ± 52	504 ± 26[e]	0	0
NGC 1614	674 ± 14	1471 ± 62[d]	800 ± 330	(54 ± 13)%

[a]For galaxies that were not mapped, conversions from K(T_A^*) to Jy were done assuming the source is point-like compared to the single dish beam, except for Arp 55 for which a main beam efficiency $\eta_{MB} = 0.63$ was used. The flux for NGC 6240 is taken from Greve et al. (2007).

[b]Uncertainty in missing flux assumes 20% calibration uncertainty on each flux except for NGC 5258 and Arp 299, for which a 30% calibration uncertainty in the JCMT data is assumed.

[c]Flux is from a single spectrum centered near the south-western source.

[d]Flux is calculated from a 7x7 map with 5" spacing.

[e]Flux is calculated from a map made with HARP-B with 6" spacing.

Table 5. **Interferometric and Single Dish 880 μm continuum fluxes**

Galaxy	JCMT flux[a] (mJy)	CO3-2[b] (mJy)	SMA flux (mJy)	Missing Flux[c] (mJy)	Percent[c] missing flux
IRAS 17208-0014	137±41	18.9	48±10	70±31	(59±14)%
Mrk 231	69±13	9.2	80±4	0	0
Mrk 273	60±16	8.4	56±5	0	0
IRAS 10565+2448	54±12	9.0	15±3	30±15	(67±13)%
UGC 5101	102±18	9.4	37±9	56±30	(60±17)%
Arp 299	376±10	93.7	101±7	181±69	(64±10)%
Arp 55	58±12	≥8.1	26±7	≤23±18	(≤47±22)%
Arp 193	100±13	21.4	39±4	40±24	(50±16)%
NGC 6240	133±40	61.4	33±13	38±30	(54±22)%
VV 114	181±8	56.7	26±6	99±33	(79±07)%
NGC 5331	64±6	9.2	27±6	28±15	(50±18)%
NGC 2623	81±12	11.9	50±2	19±21	(27±23)%
NGC 5257	101±20	8.4	<26	>66±28	(>72±17)%
NGC 5258	150±28	16.4	104±21	29±46	(22±29)%
NGC 1614	194±29	28.2	27±7	139±45	(84±6)%

[a]See text for a description of the source of the uncertainty listed here for each galaxy.

[b]SMA CO J=3-2 fluxes used for Mrk 273, NGC 5258, and NGC 5331. Arp 55 flux is likely underestimated since spectrum was centered near the south-western source and so misses most emission from the stronger north-eastern source.

[c]Uncertainty in missing flux assumes 20% calibration uncertainty on each flux.

Table 6. **Gas and dust masses from total luminosity**

Galaxy	D_L (Mpc)	$L'_{CO}(3-2)$ (10^9 K km s^{-1} pc^2)	T_D[a] (K)	M_{dust} (10^7 $M_\odot$)	M_{H_2}[b] (10^9 $M_\odot$)	Gas/Dust
IRAS 17208-0014	189	4.46	41.3	4.32 ± 0.90[c]	7.13 ± 0.49	165 ± 36[c]
Mrk 231	179	2.58	43.1	7.67 ± 0.38[d]	4.12 ± 0.11	54 ± 3[d]
Mrk 273	166	3.19	43.0	6.17 ± 0.55[e]	5.10 ± 0.16	83 ± 8[e]
IRAS 10565+2448	191	1.94	38.6	2.50 ± 0.50	3.11 ± 0.11	124 ± 25
UGC 5101	174	1.66	35.5	5.67 ± 1.38[e]	2.65 ± 0.13	47 ± 11[e]
IC 694 (Arp 299)	44	0.840	41.5	0.655 ± 0.040[e]	1.34 ± 0.02	205 ± 13[e]
NGC 3690 (Arp 299)	44	0.311	41.5	0.162 ± 0.040	0.497 ± 0.014	308 ± 77
Arp 55(NE)	173	0.737	34.5	4.09 ± 1.10	1.18 ± 0.11	29 ± 8
Arp 55(SW)	173	0.408	34.5	< 1.26 ± 0.63	0.652 ± 0.100	> 52 ± 27
Arp 193=IC883	102	2.45	35.4	2.06 ± 0.21	3.92 ± 0.07	190 ± 20
NGC 6240	107	7.39	40.4	1.63 ± 0.64	11.82 ± 0.25	725 ± 286
VV 114	87	3.09	39.4	0.876 ± 0.202	4.94 ± 0.05	565 ± 130
NGC 5331N	145	0.427	32.1	< 1.45 ± 0.73	0.682 ± 0.089	> 47 ± 24
NGC 5331S	145	2.22	32.1	3.27 ± 0.73	3.55 ± 0.21	109 ± 25
NGC 2623	80	1.04	39.9	1.40 ± 0.06[e]	1.66 ± 0.01	118 ± 4[e]
NGC 5257	99	0.746	36.0	< 1.27 ± 0.63	1.19 ± 0.20	> 94 ± 50
NGC 5258	99	2.23	36.0	5.07 ± 1.02[f]	3.56 ± 0.22	70 ± 15[f]
NGC 1614	69	0.860	42.5	0.313 ± 0.081[c]	1.38 ± 0.03	440 ± 114[c]

[a] T_e is the dust temperature calculated from fitting a modified blackbody function as in Klaas et al. (2001) to published data from 60 to 800 μm; see text.

[b] M_{H_2} calculated assuming CO3-2/CO1-0 = 0.5 and $M_{H_2} = 0.8 L'_{CO}(1-0)$ (Downes & Solomon 1998).

[c] Dust mass and gas-to-dust ratio have been corrected by a factor of 0.6 to account for a non-thermal contribution to the 880 μm flux. See text.

[d] Dust mass and gas-to-dust ratio have been corrected by a factor of 0.75 to account for a non-thermal contribution to the 880 μm flux. See text.

[e] There may be a non-thermal contribution to the continuum flux of this source; however, any effect on the dust mass and the gas-to-dust ratio is likely smaller than the uncertainties. See text.

[f] NGC 5258 contains an off-nuclear continuum source, whose flux is used here, while the CO J=3-2 emission comes primarily from the extended southern arm. Thus, the dust mass and gas-to-dust ratio given here are likely incorrect.

Table 7. **Gas and dust masses in a single beam**

Galaxy	$S_{CO}(3-2)$[a] (Jy beam^{-1} km s^{-1})	$L'_{CO}(3-2)$(peak)[a] (10^9 K km s^{-1} pc^2)	880 μm[a] (mJy beam^{-1})	M_{dust}[b] (10^7 $M_\odot$)	M_{H_2}[b] (10^9 $M_\odot$)	Gas/Dust
IRAS 17208-0014	217 ± 11	2.02	48 ± 10	4.32 ± 0.90[c]	3.24 ± 0.16	75 ± 16[c]
Mrk 231	193 ± 3	1.62	80 ± 4	7.67 ± 0.38[d]	2.58 ± 0.04	34 ± 2[d]
Mrk 273	300 ± 6	2.17	56 ± 5	6.17 ± 0.55[e]	3.47 ± 0.07	56 ± 5[e]
IRAS 10565+2448	78.1 ± 2.2	0.743	15 ± 3	2.50 ± 0.50	1.19 ± 0.03	48 ± 10
UGC 5101	103 ± 4	0.817	30 ± 4	4.60 ± 0.61[e]	1.31 ± 0.05	28 ± 4[e]
IC 694 (Arp 299)	877 ± 4	0.457	81 ± 5	0.655 ± 0.040[e]	0.732 ± 0.003	112 ± 7[e]
NGC 3690 (Arp 299)	309 ± 4	0.161	20 ± 5	0.162 ± 0.040	0.258 ± 0.003	159 ± 40
Arp 55(NE)	49.2 ± 3.6	0.386	21 ± 4	3.30 ± 0.63	0.617 ± 0.045	19 ± 4
Arp 55(SW)	22.5 ± 2.5	0.176	< 8 ± 4	< 1.26 ± 0.63	0.282 ± 0.031	> 22 ± 11
Arp 193	477 ± 4	1.32	39 ± 4	2.06 ± 0.21	2.11 ± 0.02	102 ± 11
NGC 6240	1120 ± 7	3.41	26 ± 8	1.28 ± 0.40	5.45 ± 0.03	424 ± 131
VV 114(east)	306 ± 3	0.618	13 ± 4	0.438 ± 0.135	0.989 ± 0.010	226 ± 70
VV 114(center)	223 ± 3	0.450	13 ± 4	0.438 ± 0.135	0.721 ± 0.010	165 ± 51
VV 114(west)	145 ± 3	0.293	< 8 ± 4	< 0.269 ± 0.134	0.469 ± 0.010	> 174 ± 87
NGC 5331N	48 ± 5	0.266	< 12 ± 6	< 1.45 ± 0.73	0.425 ± 0.044	> 29 ± 15
NGC 5331S	127 ± 6	0.704	27 ± 6	3.27 ± 0.73	1.13 ± 0.05	34 ± 8
NGC 2623	430 ± 1.3	0.735	50 ± 2	1.40 ± 0.06[e]	1.177 ± 0.004	84 ± 3[e]
NGC 5257	97 ± 11	0.253	< 26 ± 13	< 1.27 ± 0.63	0.405 ± 0.046	> 32 ± 16
NGC 5258	60 ± 10	0.157	< 30 ± 15	< 1.46 ± 0.73	0.250 ± 0.042	> 17 ± 9
NGC 1614	275 ± 4	0.351	21 ± 4	0.243 ± 0.046[c]	0.561 ± 0.008	231 ± 44[c]

[a]Values measured at the peak emission except for NGC 5258, where it is measured at the peak in the nuclear region. See Table 2 for the beam size for each galaxy.

[b]M_{H_2} and M_{dust} are calculated with the same assumptions and dust temperature used in Table 6.

[c]Dust mass and gas-to-dust ratio have been corrected by a factor of 0.6 to account for a possible non-thermal contribution to the 880 μm flux. See text.

[d]Dust mass and gas-to-dust ratio have been corrected by a factor of 0.75 to account for a non-thermal contribution to the 880 μm flux. See text.

[e]There may be a non-thermal contribution to the continuum flux of this source; however, any effect on the dust mass and the gas-to-dust ratio is likely smaller than the uncertaintites. See text.

Table 8. **Probability p of a false correlation after removing the effect of distance**

Quantity	$T_{\rm D}$	$\Sigma_{\rm H_2}$(peak)	beam area	$M_{\rm H_2}$(total)	$L_{\rm FIR}/M_{\rm H_2}$(total)	$L_{\rm FIR}/M_{\rm H_2}$(peak)	gas-to-dust ratio (peak)	CO J=3-2/2-1 line ratio
$L_{\rm FIR}$	**0.0168**	**0.0014**	0.0552	0.2244	**0.0250**	0.2042	0.5774	0.4554
$T_{\rm D}$	...	**0.0016**	0.0719	0.4902	**0.0321**	0.0997	0.2671	0.6234
$\Sigma_{\rm H_2}$(peak)	...	...	**0.0063**	0.2084	0.1219	0.9933	0.7035	0.7662
beam area	...	...	...	0.1202	**0.0284**	0.5258	0.5393	**0.0005**
$M_{\rm H_2}$(total)	...	...	...	...	0.2107	0.6571	0.1044	**0.0074**
$L_{\rm FIR}/M_{\rm H_2}$(tot)	...	...	...	...	...	**0.0140**	0.0916	**0.0092**
$L_{\rm FIR}/M_{\rm H_2}$(pk)	...	...	...	...	...	...	0.2411	0.2213
gas-to-dust ratio (peak)	...	...	...	...	...	...	...	0.0578

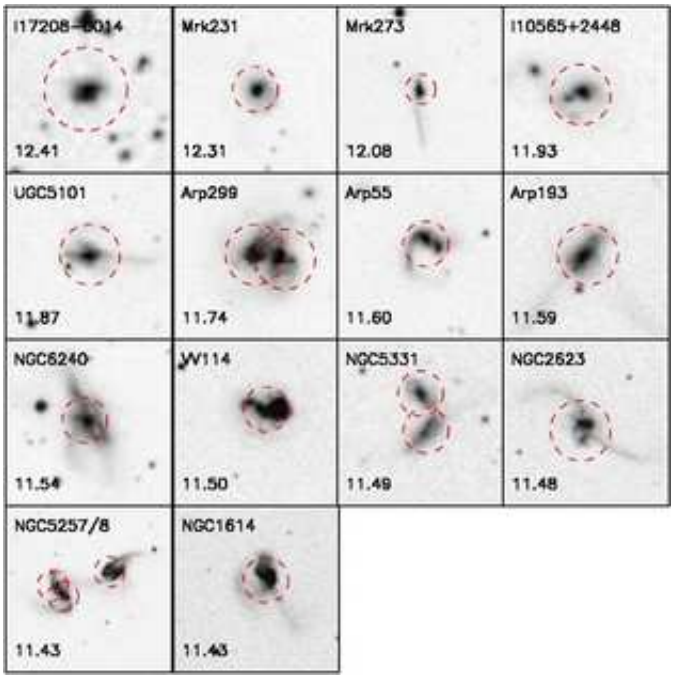

Fig. 1.— Optical images from the Second Digital Sky Survey for the fourteen galaxies in our sample with the approximate half-power beam-width field of view of the SMA at 345 GHz overlaid. Each plot is labeled with $\log L_{\rm FIR}/{\rm L}_{\odot}$. In this figure and in the tables, the galaxies are presented in order of decreasing $L_{\rm FIR}$.

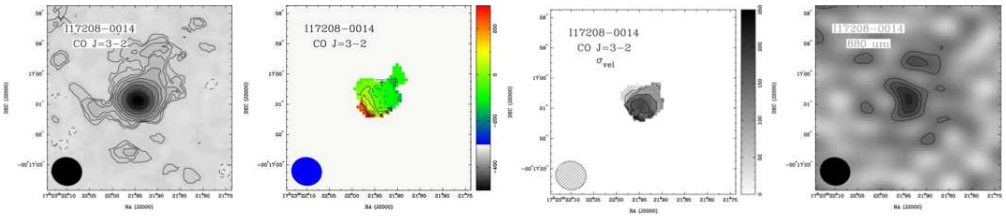

Fig. 2.— IRAS 17208-0014 CO J=3-2 and 880 μm continuum maps. See § 2 for additional details of the data processing. (a) CO J=3-2 moment 0 map. Lowest contour is 2σ = 11.4 Jy beam^{-1} km s^{-1} and contours increase by factors of 1.5. Negative contours are shown as dashed lines. The synthesized beam is shown in the lower left corner of this and subsequent panels. (b) CO J=3-2 moment 1 map. Contours are 40 km s^{-1} $\times(-5,-4,-3,-2,-1,0,1,2,3,4,5,6,7)$ relative to cz with negative contours shown as dashed lines. Because of the high noise level, for only this galaxy the moment 1 and moment 2 maps were made using 40 km s^{-1} channel maps with a 4σ flux cutoff. Note that the negative side of the rotation curve peaks at -160 km s^{-1} and then drops to -80 km s^{-1} at the extreme north-west end of the emission. (c) CO J=3-2 moment 2 map. Contours are 40 km s^{-1} $\times(1,2,3,4,5)$. This figure plots velocity dispersion, σ_v, which for a gaussian line relates to the full-width half-maximum velocity via $V_{FWHM} = 2.355\sigma_v$. (d) Uncleaned 880 μm map. Lowest contour is 2σ = 8.2 mJy and contours increase in steps of 1σ. Negative contours are not shown.

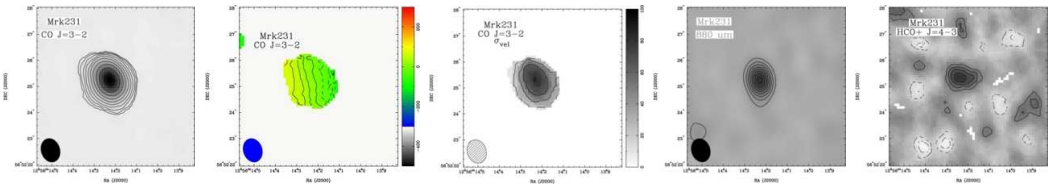

Fig. 3.— Mrk 231 CO J=3-2 and 880 μm continuum maps. Notation as in Figure 2. (a) CO J=3-2 moment 0 map. Lowest contour is 2σ = 5.2 Jy beam^{-1} km s^{-1} and contours increase by factors of 1.5. (b) CO J=3-2 moment 1 map. Contours are 20 km s^{-1} $\times(-6,-5,-4,-3,-2,-1,0,1,2,3,4)$ relative to cz. (c) CO J=3-2 moment 2 map. Contours are 20 km s^{-1} $\times(1,2,3,4)$. (d) 880 μm map. Lowest contour is 2σ = 8.2 mJy and contours increase in steps of 2σ. Because of the strength of the central source, the cleaned continuum image is shown for this galaxy only. (e) Uncleaned HCO$^+$ J=4-3 moment 0 map. Lowest contour is $\pm 2\sigma$ = 7.92 Jy beam^{-1} km s^{-1} and contours increase in steps of 1σ. This image has been corrected for continuum emission by subtracting the 880 μm continuum in the uv plane before imaging.

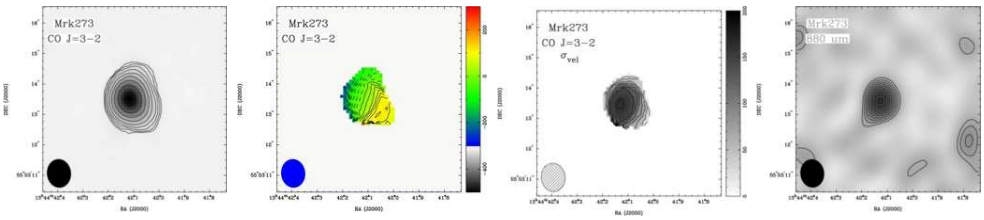

Fig. 4.— Mrk 273 CO J=3-2 and 880 μm continuum maps. Notation as in Figure 2. (a) CO J=3-2 moment 0 map. Lowest contour is 2σ = 5.2 Jy beam^{-1} km s^{-1} and contours increase by factors of 1.5. (b) CO J=3-2 moment 1 map. Contours are 20 km s^{-1} $\times(-11, -10, -9, -8, -7, -6, -5, -4, -3, -2, -1, 0, 1, 2, 3, 4, 5, 6)$ relative to cz. (c) CO J=3-2 moment 2 map. Contours are 20 km s^{-1} $\times(1, 2, 3, 4, 5, 6, 7, 8)$. (d) Uncleaned 880 μm map. Lowest contour is 2σ = 10.0 mJy and contours increase in steps of 1σ. Residual sidelobes can be seen at the edges of this figure.

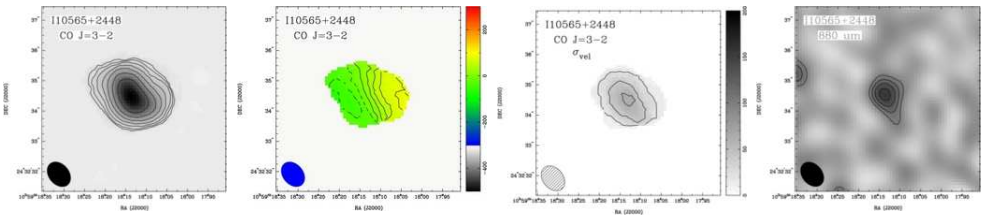

Fig. 5.— IRAS 10565 CO J=3-2 and 880 μm continuum maps. Notation as in Figure 2. (a) CO J=3-2 moment 0 map. Lowest contour is 2σ = 4.3 Jy beam^{-1} km s^{-1} and contours increase by factors of 1.5. (b) CO J=3-2 moment 1 map. Contours are 20 km s^{-1} $\times(-2, -1, 0, 1, 2, 3, 4)$ relative to cz. (c) CO J=3-2 moment 2 map. Contours are 20 km s^{-1} $\times(1, 2, 3)$. (d) Uncleaned 880 μm map. Lowest contour is 2σ = 5.4 mJy and contours increase in steps of 1σ. A residual sidelobe can be seen at the eastern edge of this figure.

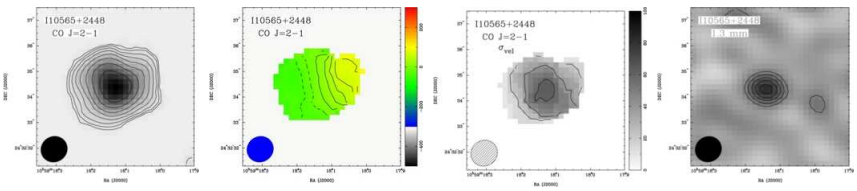

Fig. 6.— IRAS 10565 CO J=2-1 and 1.3 mm continuum maps. Notation as in Figure 2. (a) CO J=2-1 moment 0 map. Lowest contour is $\pm 2\sigma$ = 2.7 Jy beam^{-1} km s^{-1} and contours increase by factors of 1.5. (b) CO J=2-1 moment 1 map. Contours are 20 km s^{-1} $\times(-2, -1, 0, 1, 2, 3, 4)$ relative to cz. (c) CO J=2-1 moment 2 map. Contours are 20 km s^{-1} $\times(1, 2, 3)$. (d) Uncleaned 1.3 mm map. Lowest contour is 2σ = 2.0 mJy and contours increase in steps of 1σ.

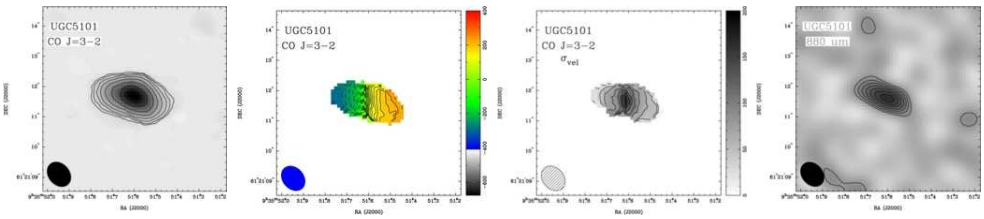

Fig. 7.— UGC 5101 CO J=3-2 and 880 μm continuum maps. Notation as in Figure 2. (a) CO J=3-2 moment 0 map. Lowest contour is $2\sigma = 7.6$ Jy beam^{-1} km s^{-1} and contours increase by factors of 1.5. (b) CO J=3-2 moment 1 map. Contours are 20 km s^{-1} $\times(-15, -14, -13, ... -2, -1, 0, 1, 2, ..., 10, 11)$ relative to cz. (c) CO J=3-2 moment 2 map. Contours are 20 km s^{-1} $\times(1, 2, 3, 4, 5, 6, 7, 8)$. (d) Uncleaned 880 μm map. Lowest contour is $2\sigma = 5.4$ mJy and contours increase in steps of 1σ. Sidelobes can be seen at the edges of this figure.

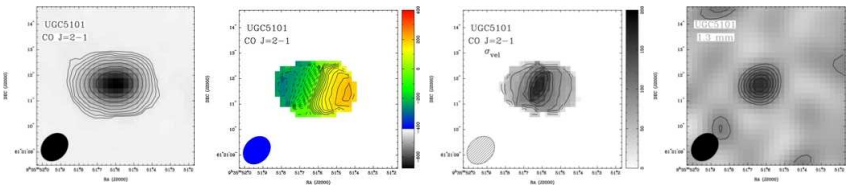

Fig. 8.— UGC 5101 CO J=2-1 and 1.3 mm continuum maps. Notation as in Figure 2. (a) CO J=2-1 moment 0 map. Lowest contour is $\pm 2\sigma = 4.6$ Jy beam^{-1} km s^{-1} and contours increase by factors of 1.5. (b) CO J=2-1 moment 1 map. Contours are 20 km s^{-1} $\times(-13, -12, -11, ... -2, -1, 0, 1, 2, ..., 8, 9, 10)$ relative to cz. (c) CO J=2-1 moment 2 map. Contours are 20 km s^{-1} $\times(1, 2, 3, 4, 5, 6, 7, 8)$. (d) Uncleaned 1.3 mm map. Lowest contour is $2\sigma = 3.0$ mJy and contours increase in steps of 1σ.

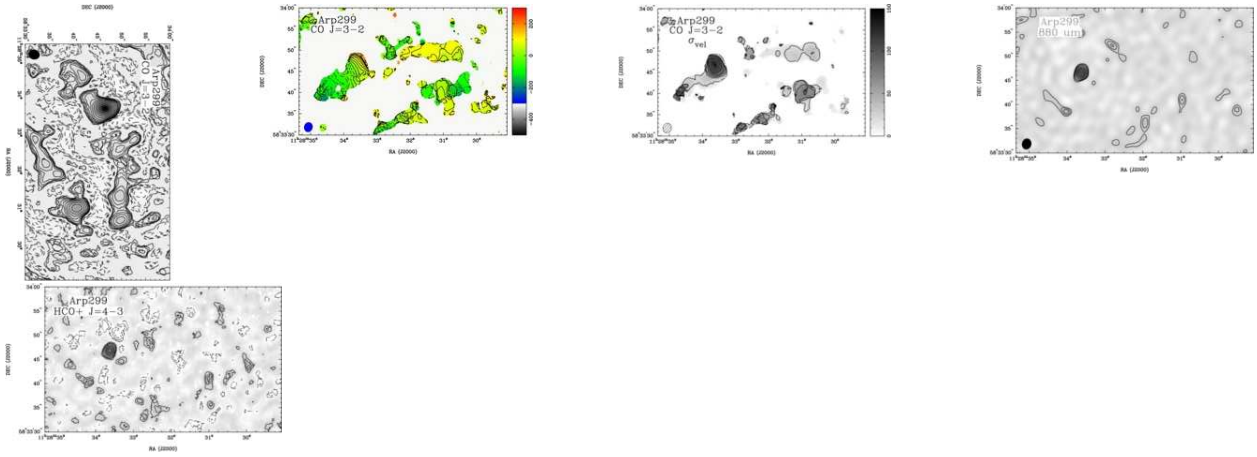

Fig. 9.— Arp 299 CO J=3-2 and 880 μm continuum maps. Notation as in Figures 2 and 3. (a) CO J=3-2 moment 0 map. Lowest contour is $\pm 2\sigma$ = 8.7 Jy beam^{-1} km s^{-1} and contours increase by factors of 1.5. (b) CO J=3-2 moment 1 map. Contours are 20 km s^{-1} $\times(-8, -7, -6, -5, -4, -3, -2, -1, 0, 1, 2, 3, 4, 5, 6, 7, 8, 9)$ relative to cz. (c) CO J=3-2 moment 2 map. Contours are 20 km s^{-1} $\times(1, 2, 3, 4, 5, 6)$. (d) Uncleaned 880 μm map. Lowest contour is 2σ = 9.8 mJy and contours increase in steps of 1σ to 4σ and then increase in steps of 2σ. (e) Uncleaned HCO$^+$ J=4-3 moment 0 map. Lowest contour is $\pm 2\sigma$ = 7.42 Jy beam^{-1} km s^{-1} and contours increase by in steps of 1σ to 4σ and then by steps of 2σ.

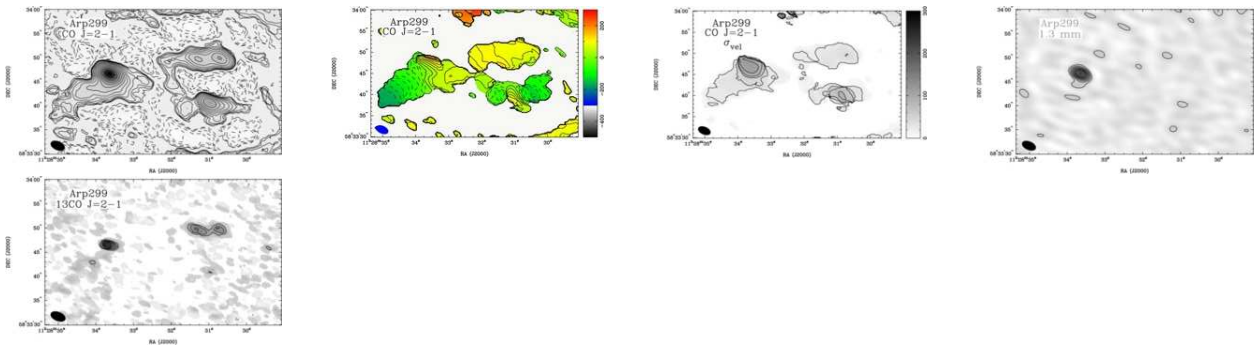

Fig. 10.— Arp 299 CO J=2-1 and 1.3 mm continuum maps. Notation as in Figure 2. (a) CO J=2-1 moment 0 map. Lowest contour is $\pm 2\sigma$ = 4.6 Jy beam^{-1} km s^{-1} and contours increase by factors of 1.5. (b) CO J=2-1 moment 1 map. Contours are 20 km s^{-1} $\times(-9, -8, -7, -6, -5, -4, -3, -2, -1, 0, 1, 2, 3, 4, 5, 6, 7, 8, 9)$ relative to cz. (c) CO J=2-1 moment 2 map. Contours are 20 km s^{-1} $\times(1, 2, 3, 4, 5)$. (d) Uncleaned 1.3 mm map. Lowest contour is 2σ = 5.4 mJy and contours increase in steps of 2σ. (e) ^{13}CO J=2-1 moment 0 map. Lowest contour is $\pm 2\sigma$ = 3.9 Jy beam^{-1} km s^{-1} and contours increase in steps of 1σ. This image has been corrected for continuum emission by subtracting the 1.3 mm continuum in the uv plane before imaging.

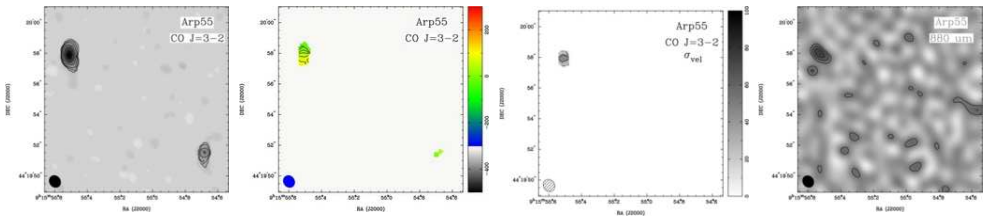

Fig. 11.— Arp 55 CO J=3-2 and 880 μm continuum maps. Notation as in Figure 2. (a) CO J=3-2 moment 0 map. Lowest contour is $2\sigma = 6.0$ Jy beam^{-1} km s^{-1} and contours increase by factors of 1.5. (b) CO J=3-2 moment 1 map. Contours are 20 km s^{-1} $\times(-1, 0, 1, 2, 3, 4)$ relative to cz. (c) CO J=3-2 moment 2 map. Contours are 20 km s^{-1} $\times(1, 2)$. (d) Uncleaned 880 μm map. Lowest contour is $2\sigma = 8.2$ mJy and contours increase in steps of 1σ.

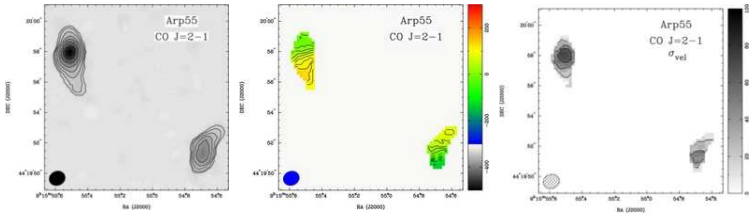

Fig. 12.— Arp 55 CO J=2-1 maps. Notation as in Figure 2. (a) CO J=2-1 moment 0 map. Lowest contour is $2\sigma = 3.4$ Jy beam^{-1} km s^{-1} and contours increase by factors of 1.5. (b) CO J=2-1 moment 1 map. Contours are 20 km s^{-1} $\times(-7, -6, -5, -4, -3, -2, -1, 0, 1, 2, 3, 4, 5, 6)$ relative to cz. Note that the positive end of the rotation curve in the north-east component peaks at 120 km/s and then drops to 100 km/s at the extreme southern end of the emission. (c) CO J=2-1 moment 2 map. Contours are 20 km s^{-1} $\times(1, 2, 3)$.

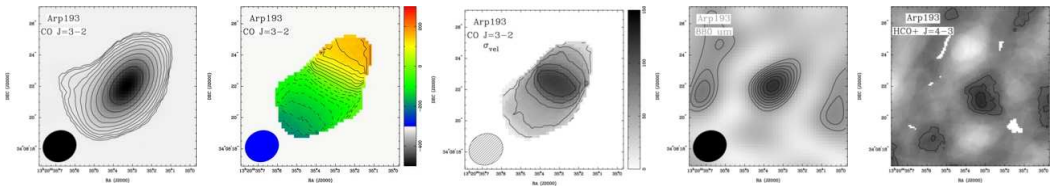

Fig. 13.— Arp 193 CO J=3-2 and 880 μm continuum maps. Notation as in Figures 2 and 3. (a) CO J=3-2 moment 0 map. Lowest contour is $2\sigma = 8.5$ Jy beam^{-1} km s^{-1} and contours increase by factors of 1.5. (b) CO J=3-2 moment 1 map. Contours are 20 km s^{-1} $\times(-9, -8, -7, -6, -5, -4, -3, -2, -1, 0, 1, 2, 3, 4, 5, 6, 7, 8, 9)$ relative to cz. (c) CO J=3-2 moment 2 map. Contours are 20 km s^{-1} $\times(1, 2, 3, 4, 5)$. (d) Uncleaned 880 μm map. Lowest contour is $2\sigma = 8.0$ mJy and contours increase in steps of 1σ. Sidelobes can be seen at the edges of this figure. (e) Uncleaned HCO$^+$ J=4-3 moment 0 map. Lowest contour is $2\sigma = 8.84$ Jy beam^{-1} km s^{-1} and contours increase by in steps of 1σ.

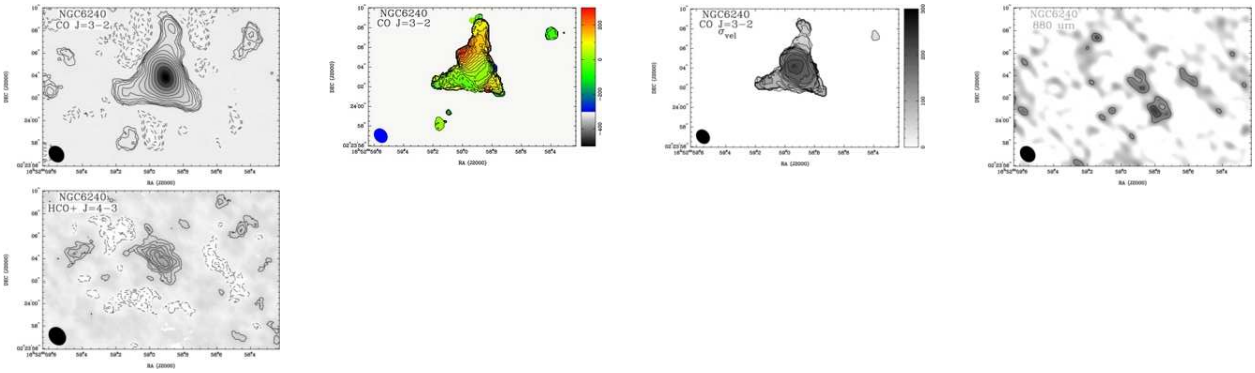

Fig. 14.— NGC 6240 CO J=3-2 and 880 μm continuum maps. Notation as in Figures 2 and 3. (a) CO J=3-2 moment 0 map. Lowest contour is $2\sigma = 12.8$ Jy beam^{-1} km s^{-1} and contours increase by factors of 1.5. (b) CO J=3-2 moment 1 map. Contours are 20 km s^{-1} $\times(-2, -1, 0, 1, 2, 3, 4, 5, 6, 7, 8, 9, 10, 11, 12, 13)$ relative to cz. (c) CO J=3-2 moment 2 map. Contours are 20 km s^{-1} $\times(1, 2, 3, 4, 5, 6, 7, 8, 9, 10, 11)$. (d) Uncleaned 880 μm map. Lowest contour is $2\sigma = 17$ mJy and contours increase in steps of 1σ. (e) Uncleaned HCO$^+$ J=4-3 moment 0 map. Lowest contour is $\pm 2\sigma = 10.22$ Jy beam^{-1} km s^{-1} and contours increase in steps of 1σ.

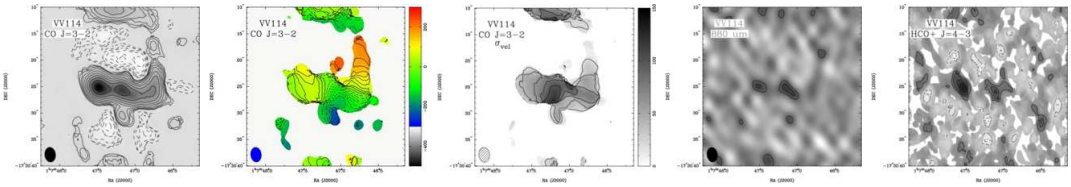

Fig. 15.— VV 114 CO J=3-2 and 880 μm continuum maps. Notation as in Figures 2 and 3. (a) CO J=3-2 moment 0 map. Lowest contour is $\pm 2\sigma = 7.0$ Jy beam^{-1} km s^{-1} and contours increase by factors of 1.5. The regions of positive emission at the extreme northern and southern edges of the image are artifacts. (b) CO J=3-2 moment 1 map. Contours are 20 km s^{-1} $\times(-12, -11, -10, ..., -2, -1, 0, 1, 2, ..., 9, 10, 11)$ relative to cz. (c) CO J=3-2 moment 2 map. Contours are 20 km s^{-1} $\times(1, 2, 3, 4, 5)$. (d) Uncleaned 880 μm map. Lowest contour is $2\sigma = 7.8$ mJy and contours increase in steps of 1σ. (e) HCO$^+$ J=4-3 moment 0 map. Lowest contour is $\pm 2\sigma = 3.68$ Jy beam^{-1} km s^{-1} and contours increase in steps of 1σ. The eastern component contains 60% of the flux given in Table 3.

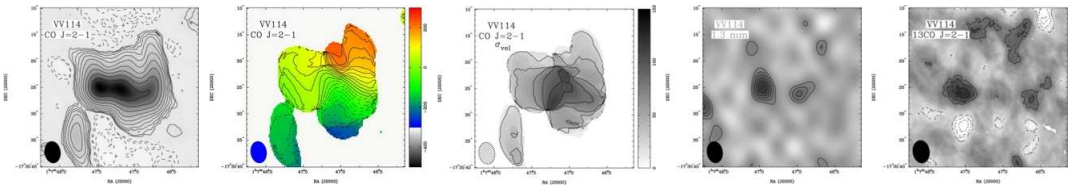

Fig. 16.— VV 114 CO J=2-1 and 1.3 mm continuum maps. Notation as in Figure 2 and 10. (a) CO J=2-1 moment 0 map. Lowest contour is $\pm 2\sigma = 3.5$ Jy beam^{-1} km s^{-1} and contours increase by factors of 1.5. (This image also has strong artifacts similar to those seen in Figure 15 but they are outside the field of view shown here.) (b) CO J=2-1 moment 1 map. Contours are 20 km s^{-1} $\times(-12, -11, -10, ..., -2, -1, 0, 1, 2, ..., 9, 10, 11)$ relative to cz. (c) CO J=2-1 moment 2 map. Contours are 20 km s^{-1} $\times(1, 2, 3, 4, 5)$. (d) Uncleaned 1.3 mm map. Lowest contour is $2\sigma = 2.6$ mJy and contours increase in steps of 1σ. (e) ^{13}CO J=2-1 moment 0 map. Lowest contour is $\pm 2\sigma = 3.2$ Jy beam^{-1} km s^{-1} and contours increase in steps of 1σ.

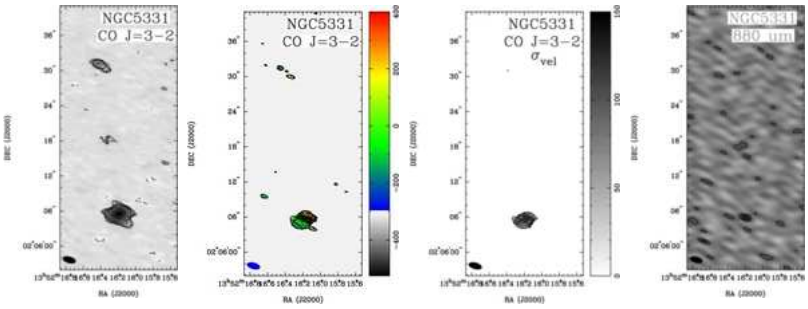

Fig. 17.— NGC 5331 CO J=3-2 and 880 μm continuum maps. Notation as in Figure 2. (a) CO J=3-2 moment 0 map. Lowest contour is $\pm 2\sigma = 21.6$ Jy beam^{-1} km s^{-1} and contours increase by factors of 1.5. (b) CO J=3-2 moment 1 map. Contours are 20 km s^{-1} $\times(-8, -7, -6, -5, ..., -2, -1, 0, 1, 2, ..., 14, 15, 16)$ relative to cz. (c) CO J=3-2 moment 2 map. Contours are 20 km s^{-1} $\times(1, 2, 3, 4, 5)$. (d) Uncleaned 880 μm map. Lowest contour is $2\sigma = 12$ mJy and contours increase in steps of 1σ.

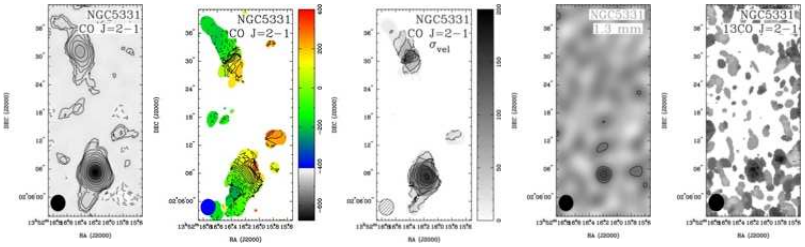

Fig. 18.— NGC 5331 CO J=2-1 and 1.3 mm continuum maps. Notation as in Figure 2 and 10. (a) CO J=2-1 moment 0 map. Lowest contour is $\pm 2\sigma$ = 5.1 Jy beam^{-1} km s^{-1} and contours increase by factors of 1.5. (b) CO J=2-1 moment 1 map. Contours are 20 km s^{-1} $\times(-12, -11, -10, ..., -2, -1, 0, 1, 2, ..., 12, 13, 14)$ relative to cz. (c) CO J=2-1 moment 2 map. Contours are 20 km s^{-1} $\times(1, 2, 3, 4, 5, 6, 7, 8)$. (d) Uncleaned 1.3 mm map. Lowest contour is 2σ = 2.6 mJy and contours increase in steps of 1σ. (e) ^{13}CO J=2-1 moment 0 map. The contour is 2σ = 4.6 Jy beam^{-1} km s^{-1}.

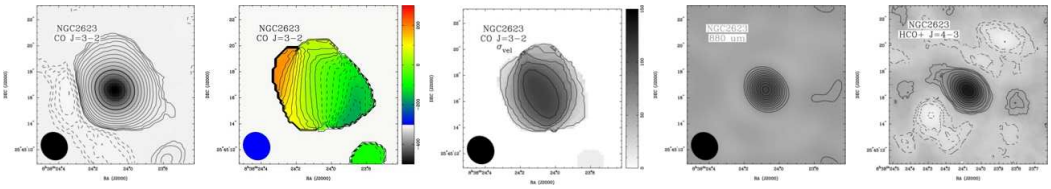

Fig. 19.— NGC 2623 CO J=3-2 and 880 μm continuum maps. Notation as in Figures 2 and 3. (a) CO J=3-2 moment 0 map. Lowest contour is $\pm 2\sigma$ = 2.7 Jy beam^{-1} km s^{-1} and contours increase by factors of 1.5. (b) CO J=3-2 moment 1 map. Contours are 20 km s^{-1} $\times(-8, -7, -6, -5, -4, -3, -2, -1, 0, 1, 2, 3, 4, 5, 6, 7, 8, 9)$ relative to cz. (c) CO J=3-2 moment 2 map. Contours are 20 km s^{-1} $\times(1, 2, 3, 4, 5)$. (d) Uncleaned 880 μm map. Lowest contour is 2σ = 4 mJy and contours increase in steps of 2σ. (e) Uncleaned HCO$^+$ J=4-3 moment 0 map. Lowest contour is $\pm 2\sigma$ = 2.60 Jy beam^{-1} km s^{-1} and contours increase in steps of 1σ to 4σ and then by steps of 2σ.

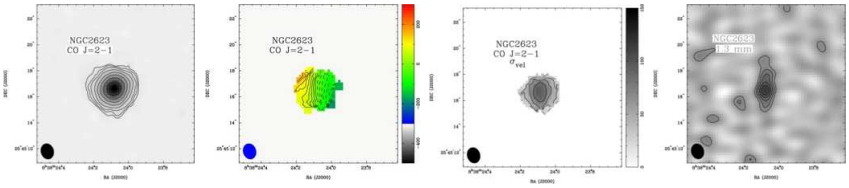

Fig. 20.— NGC 2623 CO J=2-1 and 1.3 mm continuum maps. Notation as in Figure 2. (a) CO J=2-1 moment 0 map. Lowest contour is 2σ = 4.0 Jy beam^{-1} km s^{-1} and contours increase by factors of 1.5. (b) CO J=2-1 moment 1 map. Contours are 20 km s^{-1} $\times(-9, -8, -7, -6, -5, -4, -3, -2, -1, 0, 1, 2, 3, 4, 5, 6, 7, 8)$ relative to cz. (c) CO J=2-1 moment 2 map. Contours are 20 km s^{-1} $\times(1, 2, 3, 4)$. (d) Uncleaned 1.3 mm map. Lowest contour is 2σ = 2.6 mJy and contours increase in steps of 1σ.

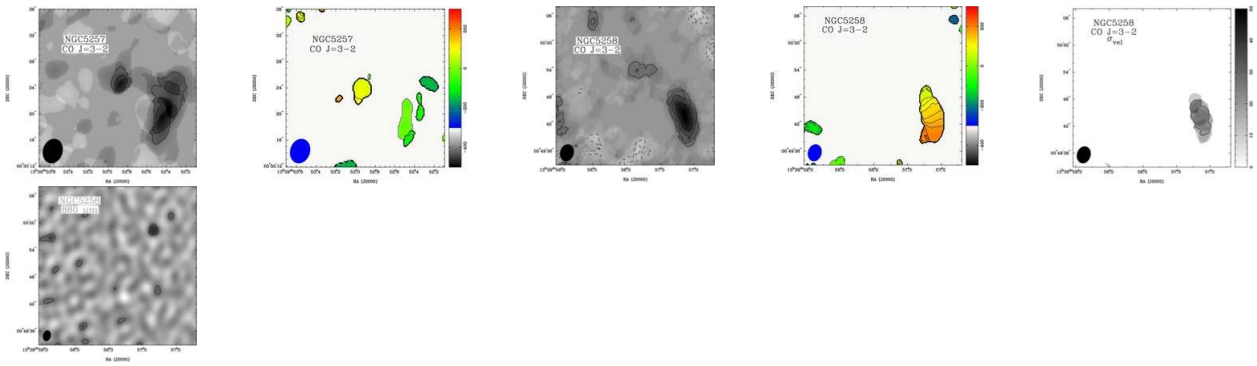

Fig. 21.— NGC 5257/8 CO J=3-2 and 880 μm continuum maps. Notation as in Figure 2. (a) CO J=3-2 moment 0 map for NGC 5257. Lowest contour is $2\sigma = 22.1$ Jy beam^{-1} km s^{-1} and contours increase by factors of 1.5. (b) CO J=3-2 moment 1 map for NGC 5257. Contours are 20 km s^{-1} $\times(0, 1, 2, 34, 5)$ relative to cz. (c) CO J=3-2 moment 0 map for NGC 5258. Lowest contour is $\pm 2\sigma = 33.7$ Jy beam^{-1} km s^{-1} and contours increase by factors of 1.5. (d) CO J=3-2 moment 1 map for NGC 5258. Contours are 20 km s^{-1} $\times(3, 4, 5, 6, 7, 8, 9, 10)$ relative to cz. (e) CO J=3-2 moment 2 map for NGC 5258. Contour is 20 km s^{-1}. (f) Uncleaned 880 μm map. Lowest contour is $2\sigma = 30$ mJy and contours increase in steps of 1σ.

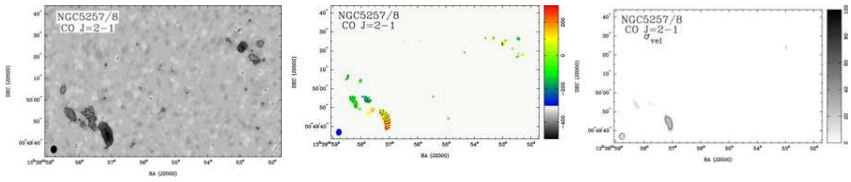

Fig. 22.— NGC 5257/8 CO J=2-1 maps. Notation as in Figure 2. (a) CO J=2-1 moment 0 map. Lowest contour is $2\sigma = 10.8$ Jy beam^{-1} km s^{-1} and contours increase by factors of 1.5. (b) CO J=2-1 moment 1 map. Contours are 20 km s^{-1} $\times(-8, -7, -6, ..., -2, -1, 0, 1, 2, ..., 8, 9, 10)$ relative to cz. (c) CO J=2-1 moment 2 map. Contour is 20 km s^{-1}.

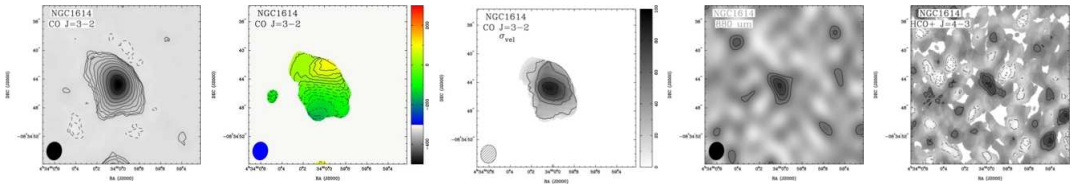

Fig. 23.— NGC 1614 CO J=3-2 and 880 μm continuum maps. Notation as in Figures 2 and 3. (a) CO J=3-2 moment 0 map. Lowest contour is $\pm 2\sigma$ = 8.2 Jy beam^{-1} km s^{-1} and contours increase by factors of 1.5. (b) CO J=3-2 moment 1 map. Contours are 20 km s^{-1} $\times(-8, -7, -6, -5, -4, -3, -2, -1, 0, 1, 2, 3, 4, 5)$ relative to cz. (c) CO J=3-2 moment 2 map. Contours are 20 km s^{-1} $\times(1, 2, 3, 4)$. (d) Uncleaned 880 μm map. Lowest contour is 2σ = 8.2 mJy and contours increase in steps of 1σ. (e) Uncleaned HCO$^+$ J=4-3 moment 0 map. Lowest contour is $\pm 2\sigma$ = 6.24 Jy beam^{-1} km s^{-1} and contours increase in steps of 1σ.

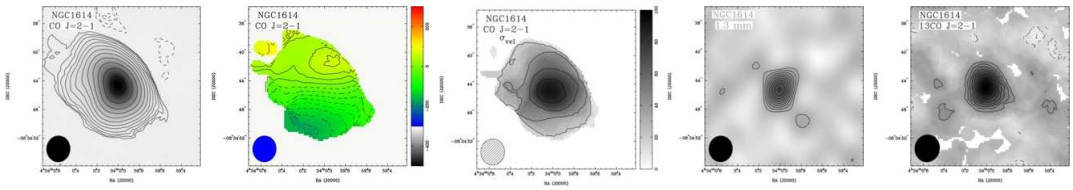

Fig. 24.— NGC 1614 CO J=2-1 and 1.3 mm continuum maps. Notation as in Figure 2 and 10. (a) CO J=2-1 moment 0 map. Lowest contour is $\pm 2\sigma$ = 3.0 Jy beam^{-1} km s^{-1} and contours increase by factors of 1.5. (b) CO J=2-1 moment 1 map. Contours are 20 km s^{-1} $\times(-8, -7, -6, -5, -4, -3, -2, -1, 0, 1, 2, 3, 4, 5)$ relative to cz. (c) CO J=2-1 moment 2 map. Contours are 20 km s^{-1} $\times(1, 2, 3, 4)$. (d) Uncleaned 1.3 mm map. Lowest contour is 2σ = 2.6 mJy and contours increase in steps of 1σ. (e) ^{13}CO J=2-1 moment 0 map. Lowest contour is $\pm 2\sigma$ = 2.5 Jy beam^{-1} km s^{-1} and contours increase in steps of 1σ.

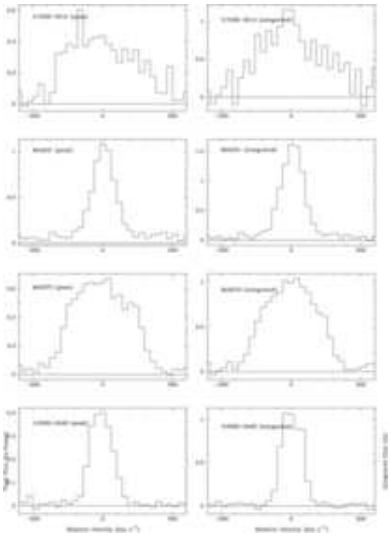

Fig. 25.— Peak and integrated spectra of the ^{12}CO J=3-2 emission for four U/LIRGs from our sample. The integrated spectrum is the sum of the emission inside a rectangular region whose size was chosen to encompass all of the emission above 2σ in the moment 0 map. The velocity scale is relative to the recession velocity for each galaxy given in Table 1.

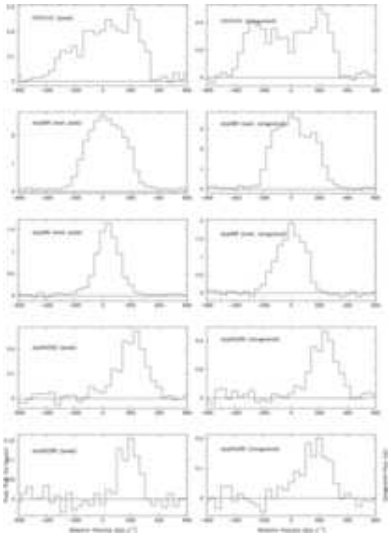

Fig. 26.— Peak and integrated spectra of the ^{12}CO J=3-2 emission for three U/LIRGs from our sample. See Figure 25 for additional details.

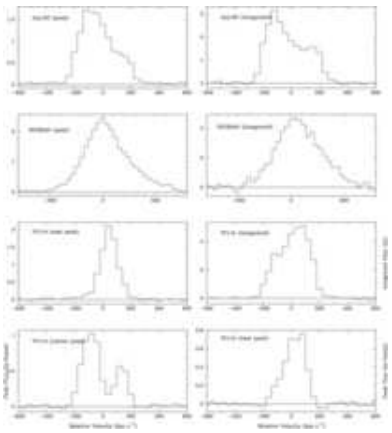

Fig. 27.— Peak and integrated spectra of the ^{12}CO J=3-2 emission for three U/LIRGs from our sample. Note the wider velocity scale used for NGC 6240. See Figure 25 for additional details.

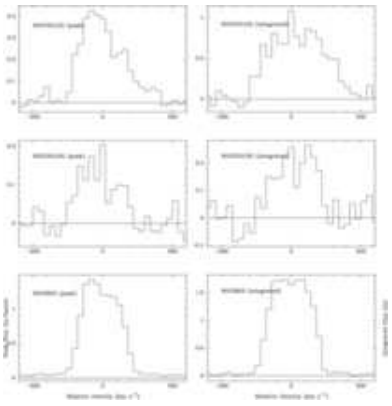

Fig. 28.— Peak and integrated spectra of the ^{12}CO J=3-2 emission for two U/LIRGs from our sample. See Figure 25 for additional details.

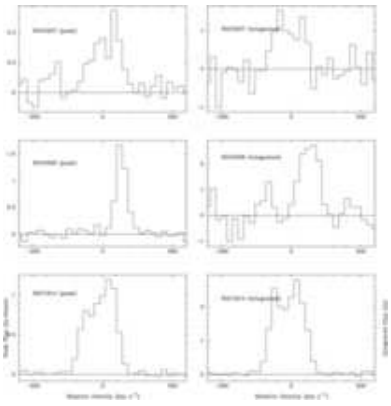

Fig. 29.— Peak and integrated spectra of the ^{12}CO J=3-2 emission for two U/LIRGs from our sample. See Figure 25 for additional details.

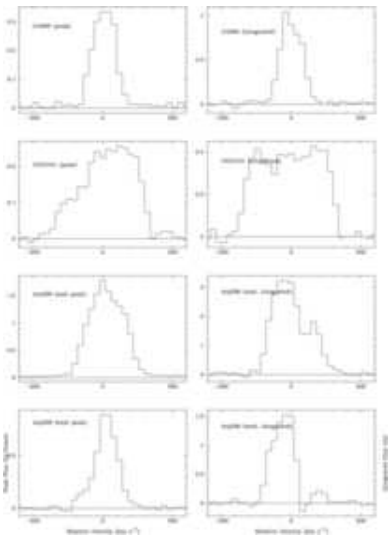

Fig. 30.— Peak and integrated spectra of the ^{12}CO J=2-1 emission for three U/LIRGs from our sample. See Figure 25 for additional details.

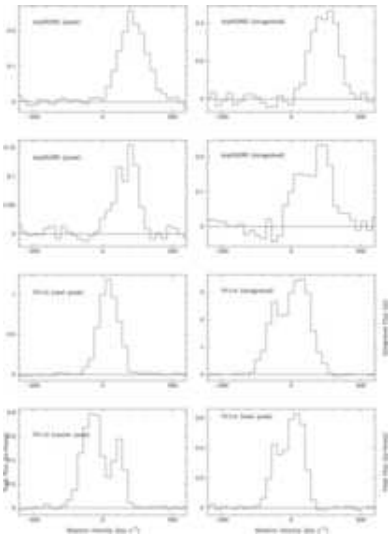

Fig. 31.— Peak and integrated spectra of the ^{12}CO J=2-1 emission for two U/LIRGs from our sample. The integrated spectrum for VV 114 encompasses the entire extended emission region. See Figure 25 for additional details.

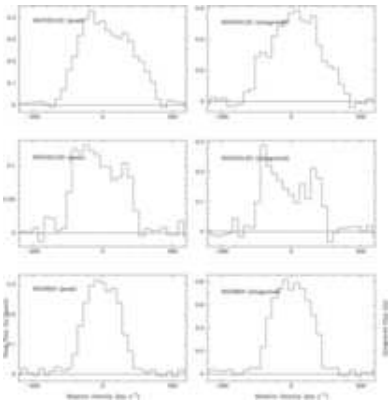

Fig. 32.— Peak and integrated spectra of the ^{12}CO J=2-1 emission for two U/LIRGs from our sample. See Figure 25 for additional details.

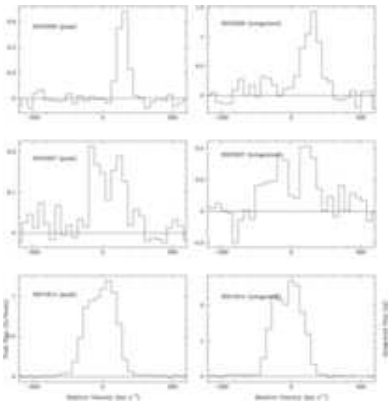

Fig. 33.— Peak and integrated spectra of the ^{12}CO J=2-1 emission for two U/LIRGs from our sample. See Figure 25 for additional details.

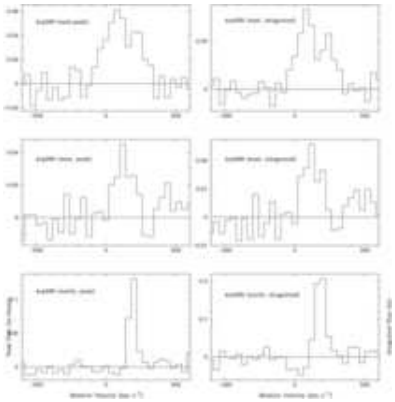

Fig. 34.— Peak and integrated spectra of the ^{13}CO J=2-1 emission for 3 regions in the interacting galaxy Arp 299 for which ^{13}CO J=2-1 emission was detected. See Figure 25 for additional details.

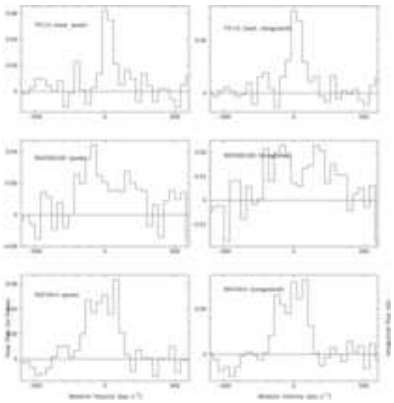

Fig. 35.— Peak and integrated spectra of the ^{13}CO J=2-1 emission for 3 U/LIRGs from our sample for which ^{13}CO J=2-1 emission was detected. See Figure 25 for additional details.

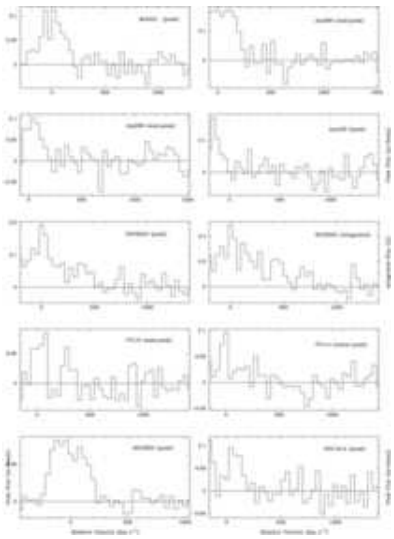

Fig. 36.— Peak spectra of the HCO^+ J=4-3 emission for nine galaxy components from our sample for which HCO^+ J=4-3 emission was detected. The integrated spectrum is also given for NGC6240. See Figure 25 for additional details.

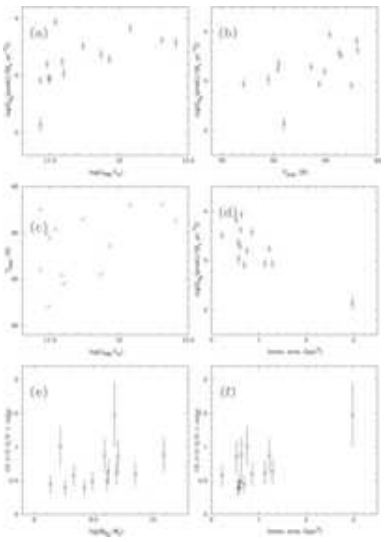

Fig. 37.— Pairs of quantities for the galaxies in our sample that showed significant correlations. (a) Peak H_2 surface density versus far-infrared luminosity. (b) Peak H_2 surface density versus dust temperature. (c) Dust temperature versus far-infrared luminosity. (d) Peak H_2 surface density versus beam area. Note that this correlation depends heavily on the two galaxies with the most divergent beam areas. (e) CO J=3-2/2-1 line ratio versus total H_2 mass detected with the SMA. (f) CO J=3-2/2-1 line ratio versus beam area.

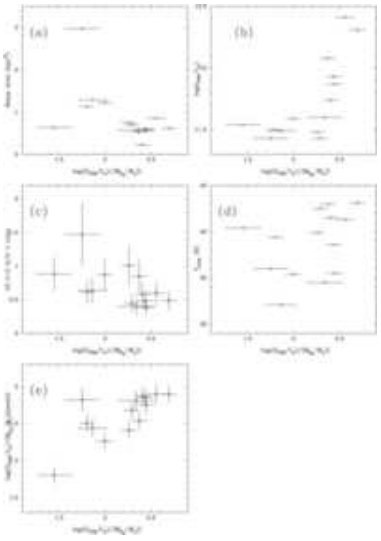

Fig. 38.— Correlations of five quantities with the ratio $L_{\rm FIR}/M_{\rm H_2}$, where $M_{\rm H_2}$ is the total mass detected with the SMA. All these correlations become insignificant if one of NGC 5257 or Arp 299 is removed from the analysis. (a) Beam area. (b) Far-infrared luminosity $L_{\rm FIR}$. (c) CO J=3-2/2-1 line ratio. (d) Dust temperature (e) Ratio of far-infrared luminosity to peak H_2 mass.

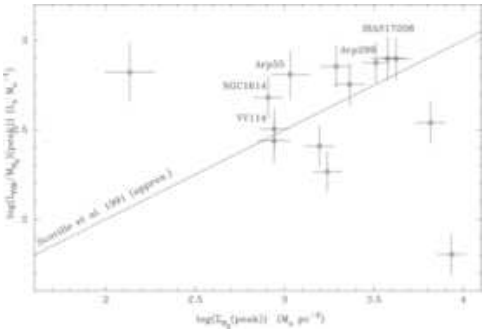

Fig. 39.— The ratio of global far-infrared luminosity to the peak H_2 gas mass detected with the SMA versus peak H_2 surface density. Only the highest surface density component is shown for composite systems. The error bars shown represent measurement errors on the CO J=3-2 emission as well as a 20% calibration uncertainty. Note that the calibration uncertainty has the same systematic effect on both quantities, since both are derived from the same data set. No correlation is seen, in conflict with the earlier study by Scoville et al. (1991). The approximate relationship seen by Scoville et al. (1991) (corrected by a factor of six to account for the different CO-to-H_2 conversion factor) is shown as the straight line. The five galaxies in common between this study and that of Scoville et al. (1991) are labeled on the plot.